Earthquake rupture and tsunami generation of the 2015 M_w 5.9 Bonin event revealed by in-situ pressure gauge array observations and integrated seismic and tsunami wave simulation

Tatsuya Kubota[1], Tatsuhiko Saito[1], Yoshio Fukao[2], Hiroko Sugioka[3], Aki Ito[2], Takashi Tonegawa[2], Hajime Shiobara[4], and Mikiya Yamashita[5]

[1]National Research Institute for Earth Science and Disaster Resilience, Tsukuba, Japan
[2]Japan Agency for Marine-Earth Science and Technology, Yokohama, Japan
[3]Kobe University, Kobe, Japan
[4]Earthqueke Research Institute, The University of Tokyo, Tokyo, Japan
[5]Geological Survey of Japan, National Institute of Advanced Industrial Science and Technology, Tsukuba, Japan

Corresponding author: T. Kubota (kubotatsu@bosai.go.jp)

Key Points:

- We examined pressure changes inside the source region of the 2015 Bonin M_w 5.9 EQ where long-period seismic waves overlap with tsunamis.
- A numerical simulation for a fluid-elastic medium was conducted for the pressure change synthetics above the seafloor.
- Analyzing both tsunamis and dynamic ground motions enabled us to estimate the stress drop and the rupture duration of the M_w 5.9 event.

Abstract

On 1 September 2015, an M_w 5.9 interplate earthquake occurred near the Bonin Trench. An array of in-situ ocean-bottom absolute pressure gauges (APGs) observed its tsunami generation field consisting of static and dynamic pressure changes due to tsunami and crustal deformation and to seismic motion, respectively, under much higher station density than ever reported. We propose an approach to synthesize the pressure change inside the focal area, which reproduces the APG waveforms well. We further successfully estimated the finite fault model of the earthquake and constrain the rupture duration only from the APG data. The relatively low stress drop and seismic wave radiation from the fault model may suggest the nature of a tsunami earthquake. The in-situ APGs have a large potential to reveal the broadband source process of the earthquake, which is essential to understand the seismotectonics in the subduction zone.

Plain Language Summary

Absolute pressure gauges (APGs) installed on the seafloor have been widely used to observe various phenomena such as tsunamis. When an APG is located inside a sub-seafloor earthquake source region, the tsunami generation field is observed, which includes not only tsunamis but also dynamic pressure changes related to seafloor dynamic motion during the earthquake fault slip. This study analyzed densely distributed APG array data, which contained the tsunami generation field of a magnitude-5.9 earthquake that happened near the Izu-Bonin Trench on 1 September 2015. This observation was performed by APG stations at higher station density than any data thus far reported. This study synthesized this APG array data using the theory for tsunami generation and propagation, and the result explained the data dramatically well. This indicates the validity of the tsunami generation theory for actual observation inside the earthquake source area. We also estimated the slip distribution across the fault of this earthquake, which could not previously be obtained. Our results indicate the combination of APG data obtained inside the focal area and the theory for tsunami generation and propagation is useful for extracting the detailed information on the earthquake rupture process.

1 Introduction

Recent developments of offshore seismic and geodetic observations have advanced our understanding of the ocean (e.g., Bürgmann & Chadwell 2014; Favali et al., 2015). The ocean-bottom absolute pressure gauge (APG) has also driven fundamental studies of tsunamis (e.g., Fukao et al., 2018; Levin & Nosov, 2009; Rabinovich & Eblé, 2015; Saito & Kubota, 2020) and seafloor geodesy (e.g., Wallace et al., 2016). Recent wide and dense offshore observation networks will drive such studies more actively (Aoi et al., 2020; Kaneda et al., 2015; Kawaguchi et al., 2015).

However, when applying conventional approaches to such new offshore data, problems often happen. For example, as the APGs have been deployed above earthquake source regions, it turned out the seafloor permanent deformation must be considered to precisely evaluate tsunamis in the APGs (Tsushima et al., 2012). APGs also observe the pressure components related to seismic waves (e.g., Filloux, 1982; Ito et al., 2020; Kubota et al., 2020a; Matsumoto et al., 2012; Nosov & Kolesov, 2007), which have been considered as noises, although recent studies have utilized these signals as seafloor seismograms to estimate centroid moment tensor (CMT) (An et al., 2017; Kubota et al., 2017). Furthermore, when APGs are installed inside the focal area, seismic and tsunami signals overlap, and thus it is not straightforward to utilize the pressure data as simple seismograms (Saito & Tsushima, 2016). Kubota et al. (2021) developed a method applicable to APGs to decompose these signals. These advancements have enabled us to utilize the broadband wave signals of the APG.

On 1 September 2015, an earthquake occurred near the Bonin Trench (hereafter, the mainshock; Figure 1a, M_w 5.8, Global CMT [GCMT]; 8 km, U.S. Geological Survey [USGS]). Its reverse-faulting mechanism with a shallow dip angle indicates the interplate earthquake between the Pacific Plate and Philippine Sea Plate. In the Izu-Bonin subduction zone, the convergence rate of the Pacific Plate is ~45 mm/yr (DeMets et al. 2010), but it is thought that the two plates are weakly coupled and most slip deficit is aseismically released (Bilek & Lay, 2018; Scholz & Campos, 1995; Uyeda & Kanamori, 1979). Similar M~6 interplate events often occur but almost no major (M >~7) interplate events have been reported (e.g., Kaiho, 1991; Plescia & Hayes, 2020). Some studies point out the possibility of $M \geq 9$ earthquakes in this region (Ikuta et al., 2015; McCaffrey, 1997; Plescia & Hayes, 2020). This M~6 mainshock will be helpful in

understanding the physics of the characteristics of the seismogenesis in the Izu-Bonin subduction zone.

When the mainshock occurred, we had installed an array of APGs just above the focal area under a much higher station density than reported ever (Figure 1a, Fukao et al., 2021), and the array recorded the tsunami generation in detail. In this study, through our integrated analysis of tsunamis and seismic waves, we estimate the mainshock rupture process and show the great advantages of the in-situ APGs for seismological studies.

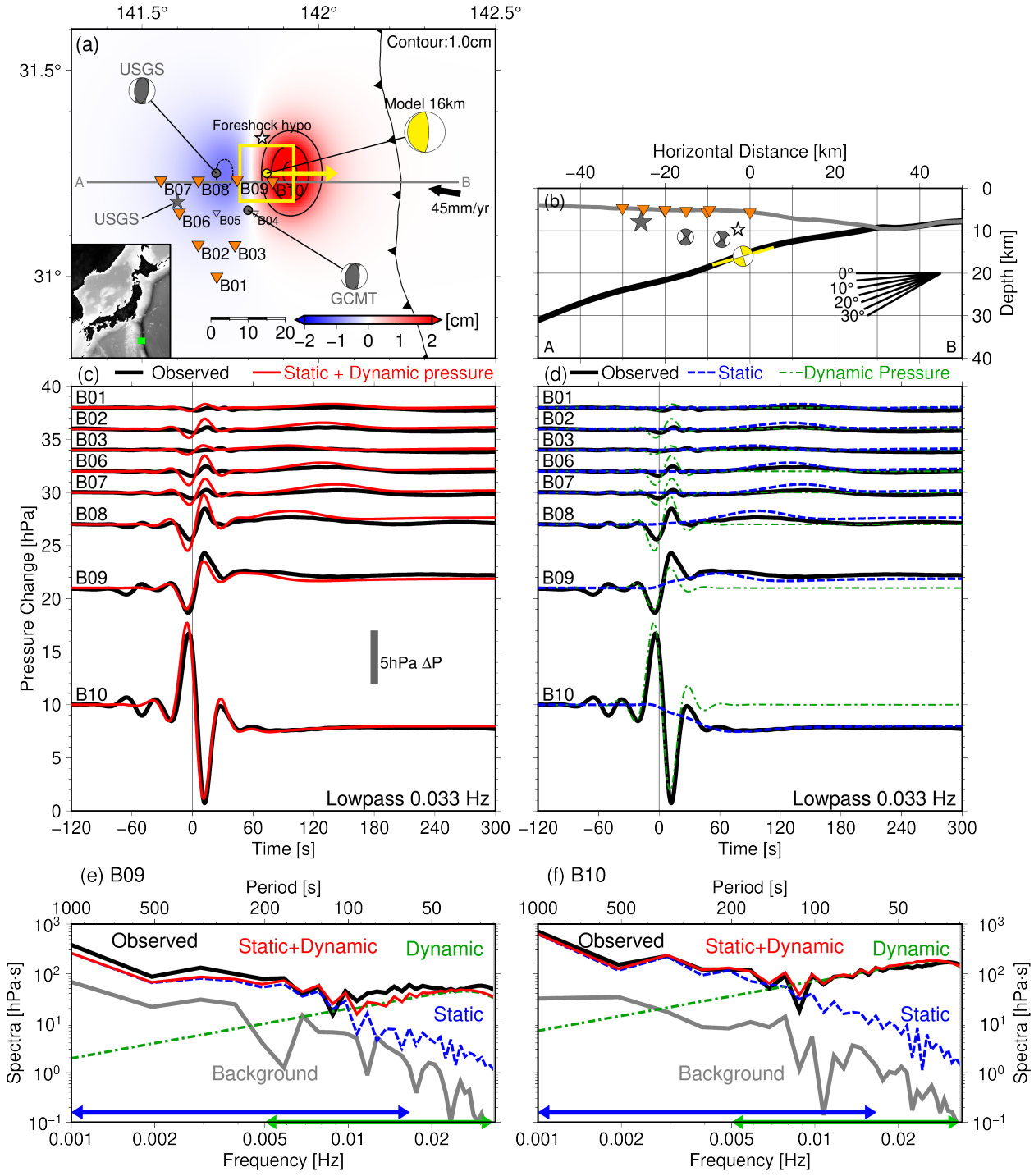

Figure 1. (a) Forward simulation results. Inverted triangles denote the stations (orange: APG available, open: unavailable). Yellow rectangle and CMT denote the location and mechanism of the fault supposed for the forward simulation, respectively. Seafloor vertical displacement expected from the supposed fault is shown by colors and contours (1-cm interval). The GCMT and USGS solutions and the USGS epicenter are shown in gray. The small white star denotes the

foreshock epicenter (Fukao et al., 2021). The black arrow denotes the plate convergence direction (DeMets et al., 2010). (b) Vertical cross section along line A-B in Figure 1a. The black line denotes the Pacific Plate surface (Iwasaki et al., 2015). (c,d) Comparisons of the observed (black) and simulated waveforms. Blue, green, and red traces are the synthetic waveforms considering only hydrostatic pressure change, only dynamic pressure change, and both, respectively. Lowpass filters with a cutoff of 0.033 Hz are applied. (e,f) Fourier spectra of the waveforms at B09 and B10. The black, gray, and colored lines are the spectra for the observation, background, and simulations, respectively. Colored allows show the frequency bands where the hydrostatic and dynamic components are dominant.

2 Data and method

2.1 Theory for tsunami generation and propagation

We briefly describe a theory of the tsunami generation and propagation. When earthquakes occur beneath seafloor, the seafloor vertically and horizontally displaces. Sea-surface also vertically displaces and then collapses and propagates due to gravity, resulting in tsunamis. The APG observes the hydrostatic pressure changes related to the tsunamis and the seafloor permanent displacement as:

$$p_{hydrostatic}(t) \approx \rho_0 g_0 \big(\eta(t) - u_z(t)\big), \quad (1)$$

where ρ_0 and g_0 are the seawater density and gravitational acceleration, and $\eta(t)$ and $u_z(t)$ are the time history of the sea-surface height (tsunami) and seafloor vertical displacement, respectively (Tsushima et al., 2012). The APGs also observe the dynamic pressure changes related to the seafloor dynamic vertical motion. The dynamic pressure change is approximately given as:

$$p_{dynamic}(t) \approx \rho_0 h_0 a_z(t), \quad (2)$$

where $a_z(t)$ is the seafloor vertical acceleration, and h_0 is the seawater depth (e.g., Filloux, 1982). This equation can be interpreted as an action-reaction force due to the vertically accelerating seafloor. Equation (2) holds when the wave frequency f is lower than the fundamental acoustic resonant frequency $f_0 = c_0/4h_0$ ($f < f_0$, c_0 ~1.5 km/s: ocean-acoustic wave velocity), enough to

consider the seawater to be incompressible (e.g., Nosov & Kolesov, 2007; Saito, 2019). Since the hydrostatic and dynamic pressure changes are generated with and without gravity, respectively, the tsunami generation field can be expressed by the sum of them (Saito & Tsushima, 2016; Saito, 2019):

$$p(t) = p_{hydrostatic}(t) + p_{dynamic}(t). \quad (3)$$

2.2 APG array observation

We installed an array of stations B01 to B10, inward of the northern Bonin Trench (Figure 1a, Table S1, Fukao et al., 2021). We use the APGs at B01–B03 and B06–B10 for which data were available. Ocean tides were removed by fitting a set of harmonic oscillation functions (Figure S1a, see Fukao et al., 2021). The APGs recorded large pressure fluctuations of up to ~0.05 MPa. Small pressure fluctuations, observed ~1 min before the focal time, are due to the foreshock (the epicenter determined by Fukao et al. (2021) is shown by small white star in Figure 1a). We also show the waveforms from the broadband ocean-bottom seismometer (BBOBS) and the differential pressure gauge (DPG) at B05 in Figure S1a. The BBOBS waveform saturated, whereas the DPG successfully recorded the whole waveform without the saturation. Note that the DPG was not used in our analyses because of its lower sensitivity to the longer-period components, such as the seafloor permanent deformation.

We then applied the acausal lowpass filter with a cutoff of 0.033 Hz (red traces in Figure S1b). The cutoff was determined so that the frequency is enough lower than the fundamental acoustic resonant frequency in this region (f_0 ~0.066 Hz, assuming h_0 = 5.5 km). Large impulsive signals related to the seismic wave were confirmed as well as those in the bandpass-filtered waveforms (0.01 to 0.033 Hz, green traces). The polarities of the first and second pulses at B10 were up and down, respectively, while the opposite feature was confirmed at B09 and other stations. Low-frequency signals attributed to the tsunamis and seafloor permanent displacements are then observed, as well as in the lowpass-filtered waveforms (≤ 0.01 Hz, blue traces).

3 Forward simulation of APG waveforms

We forwardly synthesize the APG waveforms to investigate the contributions of the hydrostatic and dynamic pressures. We assume a rectangular planer fault near B10 (yellow

158 rectangle in Figure 1a). For simplicity, we assume pure reverse-faulting slip (rake = 90° and
159 strike = 180°). Fault dip angle and depth are determined based on the plate boundary model of
160 Iwasaki et al. (2015) and Takahashi et al. (2015) (dip = 16°, center depth = 18 km, Figure 1b).
161 The horizontal location and dimension of the fault were determined after some trial and error
162 (length L = 15 km, width W = 15 km). Slip amount was set as D = 13 cm so that the observed
163 waveforms are explained (seismic moment: $M_0 = 8.8 \times 10^{17}$ Nm, μ = 30 GPa).

164 Although there are some approaches based on the coupled simulations of the seismic
165 waves and tsunamis (e.g., Kozdon & Dunham, 2013; Lotto & Dunham, 2015; Madden et al.,
166 2021; Maeda & Furumura, 2013; Wilson & Ma, 2021), we adopted a simpler approach. The
167 procedure is briefly explained here; see Text S1 for details. The hydrostatic pressure changes
168 (Eq. (1)) are synthesized by a conventional tsunami calculation method from a rectangular fault
169 (Kajiura, 1963; Okada, 1992; Satake, 2002). The dynamic pressure changes (Eq. (2)) are
170 converted from the seafloor vertical accelerations $a_z(t)$, synthesized based on the elastodynamic
171 equation with the conventional discrete wavenumber method (e.g., Herrmann, 2013) assuming a
172 point source at the center of the rectangular fault. In the conversion, we assume a seawater
173 density of ρ_0 = 1.03 g/cm^3 and depths h_0, as listed in Table S1. We finally combine them to
174 calculate the hydrostatic and dynamic pressure changes (Eq. (3)) and apply the same lowpass
175 filter as applied to the observation.

176 In the simulation, we assume the following source time function $\tau(t)$:

177

178 $$\tau(t) = \frac{1}{T_\mathrm{r}}\left[1 - \cos\left(\frac{2\pi t}{T_\mathrm{r}}\right)\right], \quad (4)$$

179

180 where T_r represents the duration of the source time function. Considering the GCMT duration of
181 4 s, we assumed T_r = 5.0 s.

182 Combined waveforms of the hydrostatic and dynamic pressure changes reproduced the
183 observation (red trace in Figure 1c). The forward simulation considering only the hydrostatic
184 pressure changes reproduce tsunamis and offset changes due to seafloor deformation, while the
185 dynamic pressure simulation reproduces impulsive pressure change (blue and green traces in
186 Figure 1d). We also calculate the Fourier transform of these waveforms using the time windows
187 during −300 and 600 s from the origin time, based on the definition of Aki and Richards (2002)
188 (black and colored lines in Figures 1e and 1f). The background spectra calculated using the time

window of −3,900 to −3,000 s from the origin time are also shown in gray lines. The hydrostatic pressure changes contribute to the signals in the frequency range of < ~0.01 Hz (compare gray and blue lines), while the components in the range of > ~0.01 Hz were reproduced by the dynamic pressure changes (gray and green lines). Both hydrostatic and dynamic components contributed to reproducing the signals between around 0.005–0.02 Hz.

We assess goodness of waveform reproductivity based on the root mean square error (RMSE):

$$RMSE = \sqrt{\frac{1}{N}\sum_{i=1}^{N}\left(x_i^{\mathrm{obs}} - x_i^{\mathrm{syn}}\right)^2}, \quad (6)$$

where x_i^{obs} and x_i^{syn} is the i-th data sample of the observed and synthetic waveforms, and N is the total number of the data sample. Using all the APG stations with the time window between −300 to 600 s from the origin time, we obtain RMSE = 0.32 hPa.

When assuming larger T_r, the simulated dynamic pressure changes temporally elongate and the maximum amplitudes decrease (red lines in Figures 2a and 2b), leading to larger RMSEs (green or red line in Figures 2c and 2d). On the other hand, the RMSEs considering only the hydrostatic pressure change (blue) are almost identical regardless of T_r. This indicates that the dynamic pressure is sensitive to duration and that incorporating dynamic pressure provides better temporal resolution for the rupture. The duration was not well constrained for T_r < ~20 s from the RMSE values because of the cutoff of the lowpass filter (0.033 Hz), although we constrained the duration as T_r ~7 s based on another approach shown later.

In the calculation, the frequency dispersion effect of the tsunami propagation was neglected, because the simulated pressure waveforms considering the dispersion showed its effect was minor (Figure S2). Furthermore, although the relationship $p = \rho_0 g_0 \eta$ was used to convert the tsunami height to the hydrostatic pressure (Eq. (1)), more rigorous relationship is $p = \rho_0 g_0 \eta/\cosh(kh_0)$ (k: wavenumber, e.g., Saito, 2019). Assuming the wavelength of the tsunami λ (= $2\pi/k$) from the spatial dimension of the initial tsunami height, as ~50 km, we obtain the factor of $1/\cosh(kh_0)$ ~0.8 (assuming h_0 = 5.5 km). Although we neglect this effect in the finite fault modeling shown below, this may suggest the actual seismic moment is possibly slightly larger than the estimated one.

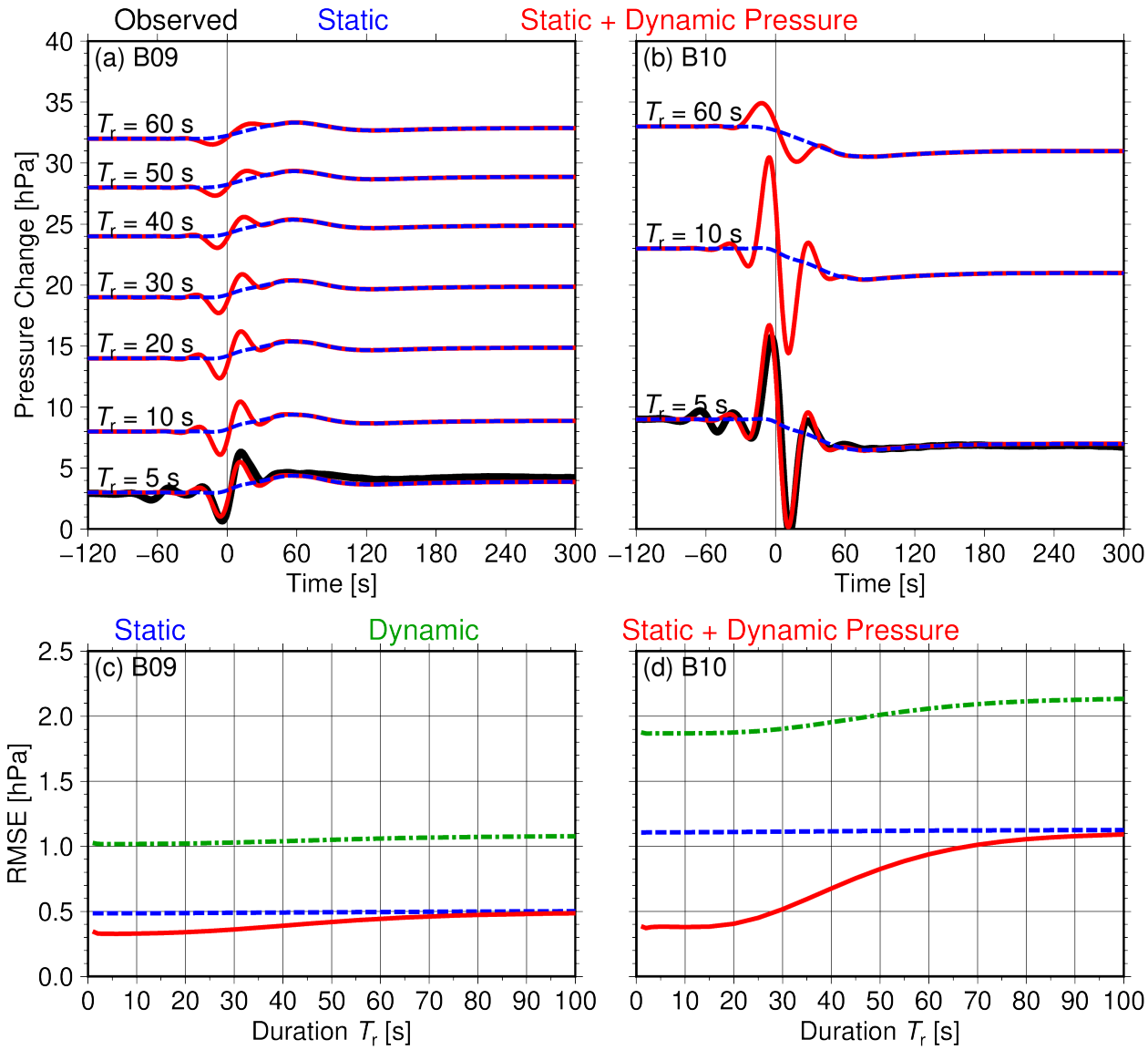

Figure 2. Relationship between the duration and the synthesized waveforms. (a,b) Comparisons of observed (black) and synthesized (colored) waveforms with different durations for (a) B09 and (b) B10. (c,d) Relationship between T_r and RMSE between the observed and simulated waveforms at (c) B09 and (d) B10. Blue, green, and red traces are the synthesized waveforms considering only hydrostatic, only dynamic, and both pressure changes, respectively.

4 Finite fault inversions

We estimated the coseismic slip distribution of the mainshock by inverting the APG data (Fukao et al., 2021; see Text S2 for details). To calculate the pressure changes from each

subfault (Green's function), we assume a planar fault with a dimension of 40 km length × 28 km width and divide it into 4 km × 4 km sub-faults. We calculate the Green's functions related to the hydrostatic pressure changes using each rectangular subfault. We also calculate the dynamic pressure change Green's functions assuming a point source at the center of each subfault. We finally combined them to calculate the Green's functions. We assume the same fault mechanism and duration as used in the forward simulation. We assume the ruptures of all subfaults begin simultaneously (i.e., infinite rupture propagation velocity), because the filter cutoff (0.033 Hz) is sufficiently low for the M~6 earthquake to neglect the rupture propagation across the fault. We impose a spatial smoothing constraint (Figure S3) and a non-negativity constraint in the inversion analysis (Lawson & Hanson, 1974).

The estimated slip distribution is plotted in Figure 3a. The location of the large slip area was consistent with the rectangular fault in the forward modeling, located at ~15 km east and ~10 km northwest from the USGS and GCMT centroids, respectively. The seismic moment of $M_0 = 9.5 \times 10^{17}$ Nm (M_w 5.9) was consistent with the USGS and GCMT solutions. The simulated waveforms from the slip model (red trace in Figure 3c) reproduced the observation (RMSE = 0.30 hPa).

To investigate the rupture characteristics of this event, we calculated the stress drop at each subfault from the slip distribution (Figure 3b). The subfaults with the slip amount D is larger than 20% of the maximum slip D_{max} (marked by black lines in Figure 3a, ~210 km^2) correspond to the region where the stress drop is positive. We also calculate the slip-weighted average of the stress drop, $\Delta\sigma_E$ (Noda et al., 2013). Using the sub-faults with $D > 0.2D_{max}$, we obtain $\Delta\sigma_E = 0.5$ MPa. We evaluate the estimation uncertainty using the mean and standard deviation based on the jackknife inversion test ($\mu \pm 1\sigma$, Figures S4 and S5, see Text S3 for details). we obtain the uncertainties of $M_0 = 8.0–11.6 \times 10^{17}$ Nm, the slip area of 208–224 km^2, and $\Delta\sigma_E = 0.46–0.50$ MPa.

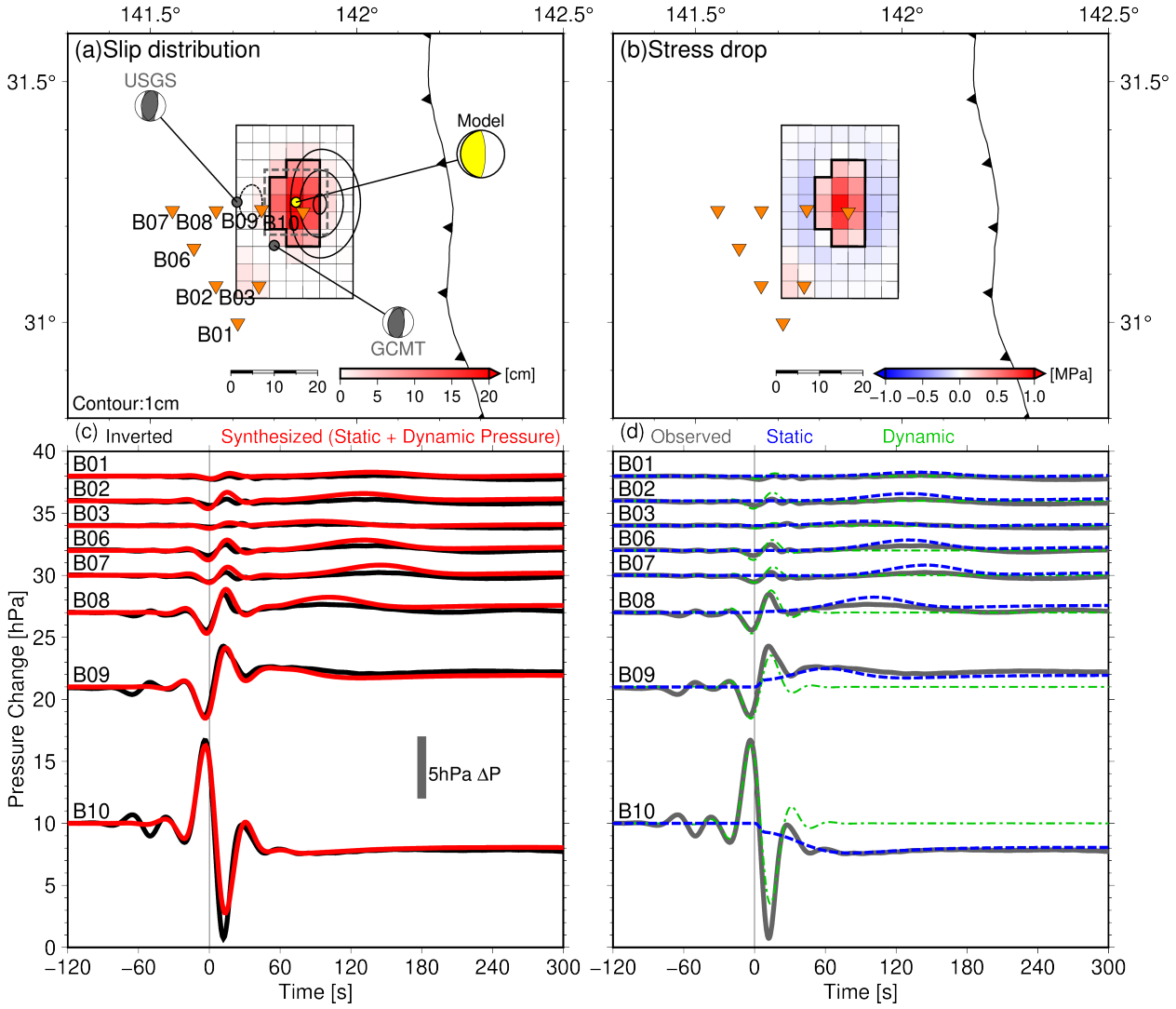

Figure 3. Result of the inversion. (a) Slip distribution (colored tiles) and seafloor vertical displacement (black contours). The area of $D > 0.2D_{max}$ is marked by thick black lines. The yellow circle and CMT solution denote the location of the centroid calculated from the slip distribution and the assumed fault mechanism, respectively. The USGS and GCMT centroids are shown by gray circles. (b) Stress drop distribution. (c) Comparisons of the inverted (black) and synthesized (red) waveforms. (d) Decomposition of the forward-calculated waveforms (blue: hydrostatic, green: dynamic pressure).

We also conduct inversions considering only either the hydrostatic or dynamic pressure changes. When considering only the Green's function related to hydrostatic pressure changes, the slip distribution resembles the original inversion (RMSE = 0.49 hPa, Figure S6), indicating that

the hydrostatic pressure contributes to the spatial constraint of the horizontal location and the horizontal extent of the rupture area. This is expected because tsunamis contain the information of the fault location and rupture extent as the tsunami source distribution (An et al., 2018; Kubota et al., 2018). On the other hand, the inversion considering only the dynamic pressure changes has a spatially broader slip region, suggesting a low constraint for the rupture extent (RMSE = 0.81 hPa, Figure S7). These inversions indicate that the hydrostatic components essentially provided the effective information on the constraint of the slip distribution.

Dynamic pressure changes attributed to the foreshock (gray star in Figure 1a) show identical polarities to the mainshock (Figure 3c). We multiply the synthesized waveform due to the mainshock by 0.1 and shifting ~1 min earlier (green line in Figure S8). This waveform fits well, indicating that the foreshock has a similar faulting mechanism to the mainshock and a seismic moment equal to 0.1 times the mainshock.

5 Discussion and conclusions

The rupture time history was not resolved well even if using the dynamic pressure changes, because the rupture duration was much shorter than the filter cutoff (30 s). However, ocean-acoustic wave signals (elastic waves propagating in the seawater), ranging much higher-frequency bands, possibly give us additional information. We attempt to estimate the duration focusing on higher frequency bands. In Figure 4, we calculate the pressure change due to the ocean-acoustic waves at the seafloor, synthesized from the isotropic stress tensor ($p = -\sigma_{xx} = -\sigma_{yy} = -\sigma_{zz}$, e.g., Saito & Tsushima, 2016; Saito et al., 2019) with the wavenumber-frequency method (Herrmann, 2013). We assume a point source at the center of the rectangular fault (yellow dot in Figure 1) and use the structural model based on the Preliminary Reference Earth Model (PREM, Dziewonski & Anderson, 1981) incorporating a 6-km seawater layer (Figure S9).

When assuming the duration $T_r = 7$ s (Eq. (4)), the simulation reproduced the observed waveform at B10 well, but the simulations with longer or shorter durations did not (Figure 4a). This indicates that the rupture duration of the mainshock is ~7 s. We note that the waveforms at the other stations were not reproduced well (Figure 4b), probably due to simple assumptions such as the point source and the structure model. To accurately reproduce the ocean-acoustic waves and thus to utilize the ocean-acoustic wave signals for the fault modeling, an appropriate

structure model optimized for the target region and incorporation of the rupture propagation across the fault are necessary, even for moderate (M~6) earthquakes.

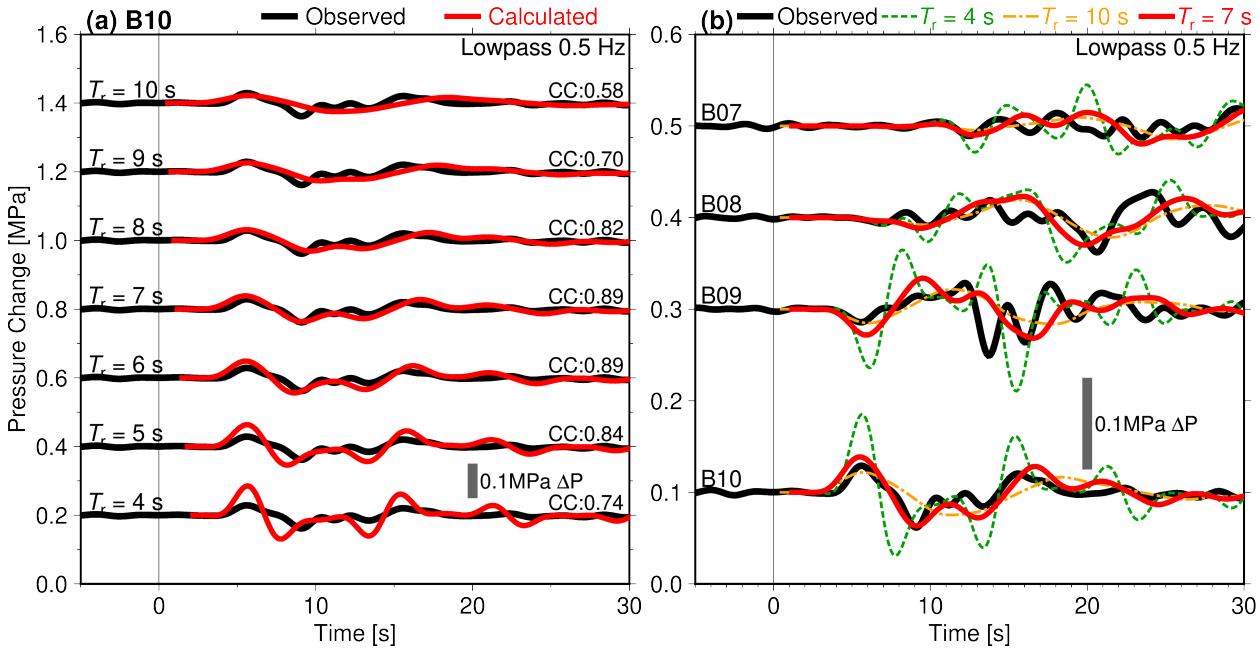

Figure 4. Comparison of the observed and simulated waveforms of the ocean-acoustic waves. (b) Observed (black) and simulated waveforms (red) at B10 with different durations T_r. The cross-correlation coefficients between the observation and simulation (CC) are also shown. (b) Waveforms at representative stations. Lowpass filters with a cutoff of 0.5 Hz are applied. The origin time of the simulations is manually shifted.

The mainshock occurred at the plate boundary near the trench axis. It is often reported that "tsunami earthquakes" (e.g., Kanamori, 1972; Tanioka & Satake, 1996) occur at the shallower portion of the plate boundary near the trench axis (Fukao, 1979). A relatively small stress drop is another feature of tsunami earthquakes (Bilek et al., 2016; Ye et al., 2016). The stress drop of the mainshock ($\Delta\sigma_E$= 0.46–0.50 MPa) is slightly small compared with those expected in ordinary interplate earthquakes (~10^0 MPa). Considering the fault length of ~15 km and duration of T_r ~ 7 s, the rupture velocity across the fault can be approximated as ~2 km/s supposing unilateral rupture propagation. We further estimate the radiation energy E_R and radiation efficiency E_R/M_0 (Venkataraman & Kanamori, 2004), assuming the ω^{-2} moment rate spectrum model (Aki, 1967) with a corner frequency of $f_c = 1/T_r = 0.14$ Hz (see Text S3 for

details). We obtain $E_R = 1.77 \times 10^{12}$ Nm and $E_R/M_0 = 1.87 \times 10^{-6}$. When taking account of the uncertainty of these estimations, the upper limits of the possible ranges are estimated as $E_R \leq 2.7 \times 10^{12}$ Nm and $E_R/M_0 \leq 3.3 \times 10^{-6}$ (see Text S4 for details). The stress drop and radiation efficiency seem slightly smaller than those for the typical interplate earthquakes, but are rather consistent with those for tsunami earthquakes estimated from the global $M > \sim 7$ event catalog (Ye et al., 2016).

Two significant aseismic slip events were also detected in and around the rupture area of the mainshock, just after and 3.5 days after the mainshock (Fukao et al. 2021). Their magnitudes were larger than the mainshock (M_w ~6.5) and had time scales of ~1 h, which is much shorter than the characteristic duration of the typical aseismic events in this magnitude range (~days, Ide et al., 2007). Fukao et al. (2021) interpreted these aseismic events as the transitional regime between the unstable seismic-slip and stable plate-sliding regimes (Barbot, 2019). Taking the overlapping rupture areas of these aseismic slips and the mainshock into account, the mainshock rupture might have occurred under the unstable seismic-slip regime but relatively close to the transitional regime. This might indicate that the mainshock rupture was more likely to be a tsunami earthquake (unstable but close to the transitional regime) rather than an ordinary interplate earthquake (completely unstable). The mainshock rupture characteristics may be one important feature to understand the Bonin subduction zone and may be relevant to the feature of the Bonin subduction zone such as the very small coupling rate as well as and the low normal stress along the plate boundary (Scholz & Campos, 1995).

Our analyses suggested that the pressure changes due to tsunamis have an advantage in constraining earthquake source dimensions (i.e., fault length and width) and thus the stress drop, while the use of the high-frequency pressure changes due to dynamic pressure changes and ocean-acoustic waves will give constraints on the rupture duration. Particularly, the dynamic pressure components (< ~0.03 Hz) will contribute to constraining the time history for megathrust (M~9) earthquakes which have much longer rupture duration of $> 10^2$ s. We also point out another advantage of our approach, whereby the high-frequency tsunami signals ranging approximately 10^{-2} to 10^{-1} Hz can be used for fault modeling (Figures 1e and 1f). Conventional tsunami analyses cannot deal with tsunamis in the frequency range where low-frequency seismic wave signals are overlapped. The analysis incorporating the dynamic pressure changes makes it

possible to include such high-frequency tsunami signals and estimate broadband rupture characteristics of offshore earthquakes (Webb, 1998; Webb & Nooner, 2016).

It is often difficult to constrain the slip distribution of *M*~6 offshore earthquakes only from seismographs or a few APGs located far from the source region (e.g., Kubota et al., 2020b). However, our in-situ APG array enabled us to reveal the detailed mainshock rupture process. Recently, new wide offshore networks, which can observe the seismicity in the wider region with uniform quality, have been established (Aoi et al., 2020; Kaneda et al., 2015; Kawaguchi et al., 2015). On the other hand, a small APG array, as used in this study, has the advantage of revealing the smaller-scaled geodynamic phenomena. APGs have a strong advantage in that their signal never saturates, whereas the BBOBS signal often saturates (Figure S1a). Not only the wide permanent observation network, but the small temporary observation array, designed for observing specific phenomena, will be also important to understand the geodynamics in the subduction zone with high resolution. This study showed the great potential of the in-situ broadband APG array data, in which the signal never saturates, to deepen our understandings of the subduction zone processes.

Acknowledgments, Samples, and Data

We used 500 m gridded bathymetry data published by the Japan Oceanographic Data Center, Japan Coast Guard (https://www.jodc.go.jp/jodcweb/JDOSS/index.html, the information of the data is available from https://www.jodc.go.jp/jodcweb/JDOSS/infoJEGG.html). The plate boundary model by Iwasaki et al. (2015) was downloaded from http://evrrss.eri.u-tokyo.ac.jp/database/PLATEmodel/. We used the Computer Programs in Seismology (Herrmann, 2013) version 3.30 for the seismic wave propagation simulation (http://www.eas.slu.edu/eqc/eqccps.html). We used Seismic Analysis Code software version 101.6a for the data processing (Goldstein et al., 2003). We used Generic Mapping Tools version 6.2.0 (Wessel et al. 2019) to generate the figures. The station locations of the APGs are listed in Table S1 and are presented in Fukao et al. (2021). The APG data is available on the Zenodo repository (https://doi.org/10.5281/zenodo.5139450), which is the supplementary dataset of Fukao et al. (2021).

This work was supported by the Sasakawa Scientific Research Grant #2019-2037 from the Japan Science Society, by JSPS KAKENHI Grant Numbers JP25247074, JP17K05646,

JP19K14818, and JP20K04142, and by ERI JURP, 2014-G-02 and 2015-G-07. We would like to thank T. Oi for his help with the instrumentation. We would also like to thank the shipboard scientists and technical staff of cruise YK15-08 of R/V *Yokosuka* and cruise MR16-E02 of R/V *Mirai*. The English in this manuscript was edited by Forte Science Communications (www.forte-science.co.jp).

References

Aki, K. (1967). Scaling law of seismic spectrum. *Journal of Geophysical Research*, *72*, 1217–1231. https://doi.org/10.1029/JZ072i004p01217

Aki, K., & Richards, P. G. (2002). *Quantitative seismology* (2nd ed.). Mill Valley, CA: University Science Books.

An, C., Cai, C., Zheng, Y., Meng, L., & Liu, P. (2017). Theoretical solution and applications of ocean bottom pressure induced by seismic seafloor motion. *Geophysical Research Letters*, *44*, 10272–10281. https://doi.org/10.1002/2017GL075137

An, C., Liu, H., Ren, Z., & Yuan, Y. (2018). Prediction of tsunami waves by uniform slip models. *Journal of Geophysical Research: Oceans*, *123*, 8366–8382. https://doi.org/10.1029/2018JC014363

Aoi, S., Asano, Y., Kunugi, T., Kimura, T., Uehira, K., Takahashi, N., & Ueda, H. (2020). MOWLAS : NIED observation network for earthquake, tsunami and volcano. *Earth, Planets and Space*, *72*, 126. https://doi.org/10.1186/s40623-020-01250-x

Barbot, S. (2019). Slow-slip, slow earthquakes, period-two cycles, full and partial ruptures, and deterministic chaos in a single asperity fault. *Tectonophysics*, *768*, 228171. https://doi.org/10.1016/j.tecto.2019.228171

Bilek, S. L., & Lay, T. (2018). Subduction zone megathrust earthquakes. *Geosphere*, *14*, 1468–1500. https://doi.org/10.1130/GES01608.1

Bilek, S. L., Rotman, H. M. M., & Phillips, W. S. (2016). Low stress drop earthquakes in the rupture zone of the 1992 Nicaragua tsunami earthquake. *Geophysical Research Letters*, *43*, 10180–10188. https://doi.org/10.1002/2016GL070409

Bürgmann, R., & Chadwell, D. (2014). Seafloor geodesy. *Annual Review of Earth and Planetary Sciences*, *42*, 509–534. https://doi.org/10.1146/annurev-earth-060313-054953

DeMets, C., Gordon, R. G., & Argus, D. F. (2010). Geologically current plate motions. *Geophysical Journal International*, *181*, 1–80. https://doi.org/10.1111/j.1365-246X.2009.04491.x

Dziewonski, A. M., & Anderson, D. L. (1981). Preliminary reference Earth model. *Physics of the Earth and Planetary Interiors*, *25*, 297–356. https://doi.org/10.1016/0031-9201(81)90046-7

Favali, P., Beranzoli, L., De Santis, A. (Eds.). (2015). *Seafloor Observatories: a new vision of the Earth from the Abyss*. Berlin, Heidelberg: Springer. https://doi.org/ 10.1007/978-3-642-11374-1

Filloux, J. H. (1982). Tsunami recorded on the open ocean floor. *Geophysical Research Letters*, *9*(1), 25–28. https://doi.org/10.1029/GL009i001p00025

Fukao, Y. (1979). Tsunami earthquakes and subduction processes near deep-sea trenches. *Journal of Geophysical Research: Solid Earth*, *84*(B5), 2303–2314. https://doi.org/10.1029/JB084iB05p02303

Fukao, Y., Sandanbata, O., Sugioka, H., Ito, A., Shiobara, H., Watada, S., & Satake, K. (2018). Mechanism of the 2015 volcanic tsunami earthquake near Torishima, Japan. *Science Advances*, *4*(4), eaao0219. https://doi.org/10.1126/sciadv.aao0219

Fukao, Y., Kubota, T., Sugioka, Y., Ito, A., Tonegawa, T., Shiobara, H., et al. (2021) Strain release by "rapid" aseismic slip at the Izu-Bonin trench. *Journal of Geophysical Research*, *126*, e2021JB022132. https://doi.org/10.1029/2021JB022132

Goldstein, P., Dodge, D., Firpo, M., & Minner L. (2003). SAC2000: Signal processing and analysis tools for seismologists and engineers. In: W. H. K. Lee, H. Kanamori, P. C. Jennings, & C. Kisslinger (Eds.), *International Handbook of Earthquake and Engineering Seismology* (Vol. 81(B), pp. 1613–1614). London: Academic Press. https://doi.org/10.1016/S0074-6142(03)80284-X

Herrmann, R. B. (2013). Computer Programs in Seismology: An Evolving Tool for Instruction and Research. *Seismological Research Letters*, *84*, 1081–1088. https://doi.org/10.1785/0220110096

Ide, S., Beroza, G. C., Shelly, D. R., & Uchide, T. (2007). A scaling law for slow earthquakes. *Nature*, *447*, 76–79. https://doi.org/10.1038/nature05780

Ikuta, R., Mitsui, Y., Kurokawa, Y., & Ando, M. (2015). Evaluation of strain accumulation in global subduction zones from seismicity data. *Earth, Planets and Space*, *67*, 192. https://doi.org/10.1186/s40623-015-0361-5

Ito, Y., Webb, S. C., Kaneko, Y., Wallace, L. M., & Hino, R. (2020). Sea surface gravity waves excited by dynamic ground motions from large regional earthquakes. *Seismological Research Letters*. https://doi.org/10.1785/0220190267

Iwasaki, T., Sato, H., Shinohara, M., Ishiyama, T., & Hashima, A. (2015). Fundamental structure model of island arcs and subducted plates in and around Japan. Abstract T31B-2878 presented at 2015 AGU Fall Meeting, American Geophysical Union, San Francisco, CA, 14–18, Dec, 2015.

Kaiho, Y. (1991). Seismicity of the Izu-Ogasawara arc region. *Journal of Geography (Chigaku Zasshi)*, *100*(4), 503–513 (in Japanese with English abstract). https://doi.org/10.5026/jgeography.100.503

Kajiura, K. (1963). The leading wave of a tsunami. *Bulletin of the Earthquake Research Institute*, *41*, 535–571.

Kanamori, H. (1972). Mechanism of tsunami earthquakes. *Physics of the Earth and Planetary Interiors*, *6*, 346–359. https://doi.org/10.1016/0031-9201(72)90058-1

Kaneda, Y., Kawaguchi, K., Araki, E., Matsumoto, H., Nakamura, T., Kamiya, S., et al. (2015). Development and application of an advanced ocean floor network system for megathrust earthquakes and tsunamis. In P. Favali, L. Beranzoli, & A. De Santis (Eds.), *Seafloor Observatories: A new vision of the Earth from the Abyss* (pp. 643–662). Berlin, Heidelberg: Springer. https://doi.org/10.1007/978-3-642-11374-1_25

Kawaguchi, K., Kaneko, S., Nishida, T., & Komine, T. (2015). Construction of the DONET real-time seafloor observatory for earthquakes and tsunami monitoring. In P. Favali, L. Beranzoli, & A. De Santis (Eds.), *Seafloor Observatories: A New Vision of the Earth from the Abyss* (pp. 211–228). https://doi.org/10.1007/978-3-642-11374-1_10

Kozdon, J. E., & Dunham, E. M. (2013). Rupture to the trench: dynamic rupture simulations of the 11 march 2011 Tohoku earthquake. *Bulletin of the Seismological Society of America*, *103*(2B), 1275–1289. https://doi.org/10.1785/0120120136

Kubota, T., Saito, T., Suzuki, W., & Hino, R. (2017). Estimation of seismic centroid moment tensor using ocean bottom pressure gauges as seismometers. *Geophysical Research Letters*, *44*, 10907–10915. https://doi.org/10.1002/2017GL075386

Kubota, T., Saito, T., Ito, Y., Kaneko, Y., Wallace, L. M., Suzuki, S., et al. (2018). Using tsunami waves reflected at the coast to improve offshore earthquake source parameters: application to the 2016 Mw 7.1 Te Araroa earthquake, New Zealand. *Journal of Geophysical Research: Solid Earth*, *123*, 8767–8779. https://doi.org/10.1029/2018JB015832

476 Kubota, T., Saito, T., Chikasada, N.Y., & Suzuki, W. (2020a). Ultra-broadband seismic and
477 tsunami wave observation of high-sampling ocean-bottom pressure gauge covering
478 periods from seconds to hours. *Earth and Space Science*, 7, e2020ea001197.
479 https://doi.org/10.1029/2020EA001197
480 Kubota, T., Saito, T., & Suzuki, W. (2020b). Millimeter-scale tsunami detected by a wide and
481 dense observation array in the deep ocean: fault modeling of an Mw 6.0 interplate
482 earthquake off Sanriku, NE Japan. Geophysical Research Letters, 47, e2019GL085842.
483 https://doi.org/10.1029/2019GL085842
484 Kubota, T., Saito, T., Tsushima, H., Hino, R., Ohta, Y., Suzuki S, & Inazu D. (2021). Extracting
485 near-field seismograms from ocean-bottom pressure gauge inside the focal area:
486 application to the 2011 Mw 9.1 Tohoku-Oki earthquake. *Geophysical Research Letters*,
487 *48*, e2020GL091664. https://doi.org/10.1029/2020GL091664
488 Lawson, C. L., & Hanson, B. J. (1974). *Solving least squares problems*. Englewood Cliffs, NJ:
489 Prentice-Hall.
490 Levin, B. W. & Nosov, M. A. (2009). *Physics of tsunamis*. Netherlands: Springer Netherlands.
491 https://doi.org/10.1007/978-1-4020-8856-8
492 Lotto, G. C., & Dunham, E. M. (2015). High-order finite difference modeling of tsunami
493 generation in a compressible ocean from offshore earthquakes. *Computational*
494 *Geosciences*, *19*, 327–340. https://doi.org/10.1007/s10596-015-9472-0
495 Madden, E. H., Bader, M., Behrens, J., Van Dinther, Y., Gabriel, A. A., Rannabauer, L., Ulrich,
496 T., Uphoff, C., Vater, S., & Van Zelst, I. (2021). Linked 3-D modelling of megathrust
497 earthquake-tsunami events: From subduction to tsunami run up. *Geophysical Journal*
498 *International*, *224*, 487–516. https://doi.org/10.1093/gji/ggaa484
499 Maeda, T., & Furumura, T. (2013). FDM Simulation of Seismic Waves, Ocean Acoustic Waves,
500 and Tsunamis Based on Tsunami-Coupled Equations of Motion. *Pure and Applied*
501 *Geophysics*, *170*(1–2), 109–127. https://doi.org/10.1007/s00024-011-0430-z
502 Matsumoto, H., Inoue, S., & Ohmachi, T. (2012). Dynamic response of bottom water pressure
503 due to the 2011 Tohoku earthquake. *Journal of Disaster Research*, *7*, 468–475.
504 https://doi.org/10.20965/jdr.2012.p0468

McCaffrey, R. (1997). Influences of recurrence times and fault zone temperatures on the age-rate dependence of subduction zone seismicity. *Journal of Geophysical Research*, *102*(B10), 22839–22854. https://doi.org/10.1029/97jb01827

Noda, H., Lapusta, N., & Kanamori, H. (2013). Comparison of average stress drop measures for ruptures with heterogeneous stress change and implications for earthquake physics. *Geophysical Journal International*, *193*, 1691–1712. https://doi.org/10.1093/gji/ggt074

Nosov, M. A., & Kolesov, S. V. (2007). Elastic oscillations of water column in the 2003 Tokachi-oki tsunami source: in-situ measurements and 3-D numerical modelling. *Natural Hazards and Earth System Science*, *7*, 243–249. https://doi.org/10.5194/nhess-7-243-2007

Okada, Y. (1992). Internal deformation due to shear and tensile faults in a half-space. *Bulletin of the Seismological Society of America*, *82*, 1018–1040.

Plescia, S. M., & Hayes, G. P. (2020). Geometric controls on megathrust earthquakes. *Geophysical Journal International*, *222*, 1270–1282. https://doi.org/10.1093/gji/ggaa254

Rabinovich, A. B., & Eblé, M. C. (2015). Deep-Ocean Measurements of Tsunami Waves. *Pure and Applied Geophysics*, *172*, 3281–3312. https://doi.org/10.1007/s00024-015-1058-1

Saito, T. (2013). Dynamic tsunami generation due to sea-bottom deformation: Analytical representation based on linear potential theory. *Earth, Planets and Space*, *65*, 1411–1423. https://doi.org/10.5047/eps.2013.07.004

Saito, T. (2017). Tsunami generation: validity and limitations of conventional theories. *Geophysical Journal International*, *210*, 1888–1900. https://doi.org/10.1093/gji/ggx275

Saito, T. (2019). *Tsunami generation and propagation*. Tokyo: Springer Tokyo. https://doi.org/10.1007/978-4-431-56850-6

Saito, T., & Tsushima, H. (2016). Synthesizing ocean bottom pressure records including seismic wave and tsunami contributions: Toward realistic tests of monitoring systems. *Journal of Geophysical Research: Solid Earth*, *121*, 8175–8195. https://doi.org/10.1002/2016JB013195

Saito, T., & Kubota, T. (2020). Tsunami modeling for the deep sea and inside focal areas. *Annual Review of Earth and Planetary Sciences*, *48*, 6.1-6.25. https://doi.org/10.1146/annurev-earth-071719-054845

536 Saito, T., Baba, T., Inazu, D., Takemura, S., & Fukuyama, E. (2019). Synthesizing sea surface
537 height change including seismic waves and tsunami using a dynamic rupture scenario of
538 anticipated Nankai trough earthquakes. *Tectonophysics*, *769*, 228166.
539 https://doi.org/10.1016/j.tecto.2019.228166
540 Satake, K. (2002). Tsunamis. In W. H. K. Lee, P. Gennings, C. Kisslinger, & H. Kanamori
541 (Eds.), *International Handbook of Earthquake and Engineering Seismology* (pp. 437–
542 451). London: Academic Press.
543 Scholz, C. H., & Campos, J. (1995). On the mechanism of seismic decoupling and back arc
544 spreading at subduction zones. *Journal of Geophysical Research*, *100*(B11), 22103–
545 22115. https://doi.org/10.1029/95JB01869
546 Takahashi, N., Kodaira, S., Sato, T., Yamashita, M., Kaiho, Y., Miura, S., et al. (2015). Velocity
547 Structure of the Izu–Ogasawara Island Arc. *Journal of Geography (Chigaku Zasshi)*,
548 *124*(5), 813–827 (in Japanese with English abstract).
549 https://doi.org/10.5026/jgeography.124.813
550 Titov, V., Rabinovich, A. B., Mofjeld, H. O., Thomson, R. E., & Gonzalez, F. I. (2005). The
551 global reach of the 26 December 2004 Sumatra tsunami. *Science*, *309*, 2045–2048.
552 https://doi.org/10.1126/science.1114576
553 Tanioka, Y., & Satake, K. (1996). Fault parameters of the 1896 Sanriku tsunami earthquake
554 estimated from tsunami numerical modeling. *Geophysical Research Letters*, *23*, 1549–
555 1552. https://doi.org/10.1029/96GL01479
556 Tsushima, H., Hino, R., Tanioka, Y., Imamura, F., & Fujimoto, H. (2012). Tsunami waveform
557 inversion incorporating permanent seafloor deformation and its application to tsunami
558 forecasting. *Journal of Geophysical Research*, *117*, B03311.
559 https://doi.org/10.1029/2011JB008877
560 Uyeda, S., & Kanamori, H. (1979). Back-arc opening and the mode of subduction. *Journal of*
561 *Geophysical Research*, *84*(B3), 1049–1061. https://doi.org/10.1029/JB084iB03p01049
562 Wallace, L. M., Webb, S. C., Ito, Y., Mochizuki, K., Hino, R., Henrys, S., et al. (2016). Slow slip
563 near the trench at the Hikurangi subduction zone, New Zealand. *Science*, *352*, 701–704.
564 https://doi.org/10.1126/science.aaf2349
565 Webb, S. C. (1998). Broadband seismology and noise under the ocean. *Reviews of Geophysics*,
566 *36*, 105–142. https://doi.org/10.1029/97RG02287

Webb, S. C., & Nooner, S. L. (2016). High-resolution seafloor absolute pressure gauge measurements using a better counting method. *Journal of Atmospheric and Oceanic Technology*, *33*, 1859–1874. https://doi.org/10.1175/JTECH-D-15-0114.1

Wessel, P., Luis, J. F., Uieda, L., Scharroo, R., Wobbe, F., Smith, W. H. F., & Tian, D. (2019). The generic mapping tools version 6. *Geochemistry, Geophysics, Geosystems*, *20*, 5556–5564. https://doi.org/ 10.1029/2019GC008515

Venkataraman, A., & Kanamori, H. (2004). Effect of directivity on estimates of a radiated seismic energy. *Journal of Geophysical Research: Solid Earth*, *109*, B04301. https://doi.org/10.1029/2003JB002548

Wilson, A., & Ma, S. (2021). Wedge plasticity and fully coupled simulations of dynamic rupture and tsunami in the Cascadia Subduction zone. *Journal of Geophysical Research: Solid Earth*, *126*, e2020JB021627. https://doi.org/10.1029/2020JB021627

Ye, L., Lay, T., Kanamori, H., & Rivera, L. (2016). Rupture characteristics of major and great ($M_w \geq 7.0$) megathrust earthquakes from 1990 to 2015: 1. Source parameter scaling relationships. *Journal of Geophysical Research: Solid Earth*, *121*, 826–844. https://doi.org/10.1002/2015JB012426

Journal of Geophysical Research: Solid Earth

Supporting Information for

Earthquake rupture and tsunami generation of the 2015 Mw 5.9 Bonin event revealed by in-situ pressure gauge array observation and integrated seismic and tsunami wave simulation

Tatsuya Kubota[1], Tatsuhiko Saito[1], Yoshio Fukao[2], Hiroko Sugioka[3], Aki Ito[2], Takashi Tonegawa[2], Hajime Shiobara[4], and Mikiya Yamashita[5]

[1]National Research Institute for Earth Science and Disaster Resilience

[2]Japan Agency for Marine-Earth Science and Technology

[3]Kobe University

[4]Earthqueke Research Institute, The University of Tokyo

[5]Geological Survey of Japan, National Institute of Advanced Industrial Science and Technology

Contents of this file

Introduction

The procedure to synthesize the pressure waveform is described in Text S1. Text S2 presents a procedure of the inversion for the coseismic slip distribution. The procedure and result for the jackknife inversion test are described in Text S3. The procedure to calculate the radiated energy is described in Text S4. Figure S1 shows the data processing of the APG waveforms. Comparison of the forward simulated hydrostatic pressure with and without considering the dispersion effect is shown in Figure S2. Figure S3 is a trade-off curve between the smoothing weight and the RMSE value used to determine the smoothing weight in the inversion analysis. The result for the jackknife inversion test is shown in Figures S4 and S5. The inversion results using the Green's function incorporating only the tsunami and only the dynamic pressure change, are shown in Figures S6 and S7, respectively. Figure S8 depicts a comparison between the observed waveform and the forward-calculated waveforms. Figure S9 shows the structure model used for the forward calculation of the ocean-acoustic waves. Table S1 lists the location of the APG stations used in this study.

Text S1.

This text explains the procedure to synthesize the APG waveforms containing static and dynamic pressure changes. Although there is an approach to synthesize the pressure change inside the focal area based on the fully coupled simulation of the seismic waves and tsunamis (e.g., Kozdon & Dunham, 2013; Lotto & Dunham, 2015; Madden et al., 2021; Maeda & Furumura, 2013; Saito et al., 2019), we adopted a simpler approach integrating conventional calculation methods.

In this model, we assume pure-reverse faulting slip (rake = 90°) with a strike of 180° for simplicity. We also assume a dip of 16° and the fault center depth measured from sea surface at 16 km, which are determined based on the plate boundary model of Iwasaki et al. (2015) and Takahashi et al. (2015). After some trial and error, we set the fault dimension of L = 15 km and W = 15 km, and slip amount of D = 13.3 cm (seismic moment: $M_0 = 9.0 \times 10^{17}$ Nm, μ = 30 GPa). We first calculate the static pressure change from the rectangular fault model. The seafloor vertical displacement is calculated with an elastic half-space (Okada, 1992). In this calculation, we assumed the depth of the center of the rectangular fault is assumed at 16 km, but the depth from the free surface (i.e., seafloor) of the half-space was set as 10 km considering a water depth of 6 km (average depth of this region). We then incorporate the spatial filtering effect due to seawater of 6 km in depth for the seafloor displacement (Kajiura 1963; Saito, 2019) to calculate the sea-surface displacement. Using the sea-surface displacement as an initial condition, we simulate a tsunami by solving the following linear long wave equation (e.g., Satake, 2002):

$$\begin{aligned} &\frac{\partial M}{\partial t} + g_0 h_0 \frac{\partial \eta}{\partial x} = 0 \\ &\frac{\partial N}{\partial t} + g_0 h_0 \frac{\partial \eta}{\partial y} = 0, \\ &\frac{\partial \eta}{\partial t} = -\frac{\partial M}{\partial x} - \frac{\partial N}{\partial y} \end{aligned} \tag{S1}$$

where the variable η is the sea surface height anomaly (tsunami height), M and N are the velocity components integrated along the vertical direction over the seawater depth, h_0 is the water depth, and g_0 =9.8 m/s^2 is the gravitational constant. In this calculation, we used the bathymetry data published by the Japan Oceanographic Data Center (JODC), Japan Coast Guard (JCG), with a spatial interval of Δx = 500 m. The temporal interval for the simulation was set as Δt = 1 s. The sea-surface height change and seafloor vertical displacement are then converted to the static pressure change using the following relationship:

$$p_{hydrostatic}(t) \approx \rho_0 g_0 \big(\eta(t) - u_z(t)\big), \tag{S2}$$

where ρ_0 is the seawater density, and $\eta(t)$ and $u_z(t)$ are the time history of the sea-surface height (tsunamis) and seafloor vertical displacement, respectively. Here, we assumed that a 1 cm change of seawater column height ($\eta(t) - u_z(t)$) is converted to a hydrostatic pressure change of 1hPa (i.e., $\rho_0 g_0$ = 1 hPa/cm).

We then synthesize the dynamic pressure change. Assume a point source at the center of the rectangular fault with the same focal mechanism and the same seismic moment, we calculate seafloor vertical accelerogram $a_z(t)$ using a conventional elastodynamic equation with discrete wavenumber method (e.g., Herrmann, 2013). To keep the consistency with the seafloor displacement calculation in the tsunami simulation, we use a simplified half-space structure model with V_P = 7.00 km/s, V_S = 4.04 km/s, and ρ = 2.45 g/cm^3. The seafloor vertical accelerogram is then converted to the dynamic pressure change using the following relationship:

$$p_{dynamic}(t) \approx \rho_0 h_0 a_z(t). \quad \text{(S3)}$$

Here, we assumed a seawater density of 1.03 g/cm^3. The station depths (h_0 in equation (S3)) are listed in Table S1 as well as in Fukao et al. (2021). We finally combine the synthesized static and dynamic pressure waveforms:

$$p(t) = p_{hydrostatic}(t) + p_{dynamic}(t). \quad \text{(S4)}$$

We used the impulse response function in the calculations for the static and dynamic pressure changes described above. To incorporate the effects of the rupture duration, the time function $\tau(t)$ is convolved, as follows:

$$y(t) = \int y_{impulse}(t')\tau(t - t')dt', \quad \text{(S5)}$$

$$\tau(t) = \frac{1}{T_r}\left[1 - \cos\left(\frac{2\pi t}{T_r}\right)\right], \quad \text{(S6)}$$

where $y_{impulse}(t)$ is the synthesized waveform with the impulse response and T_r is the length of the base of the time function (i.e. rupture duration). We adopted T_r = 5 s. We finally apply the same lowpass filter as applied to the observation.

Text S2.

In the inversion analysis, we adopt the following observation equation:

$$\begin{pmatrix} \mathbf{x}^{\mathrm{obs}} \\ \mathbf{0} \end{pmatrix} = \begin{pmatrix} \mathbf{G} \\ \alpha\mathbf{S} \end{pmatrix} \mathbf{u}, \tag{S7}$$

where $\mathbf{x}^{\mathrm{obs}}$ is the data vector, **G** is the matrix consisting of the Green's function, **S** is the constraint matrix for spatial smoothing, and **u** is a vector representing the fault slip amount.

In the inversion, we assumed a planer fault with a dimension of 40 km length × 28 km width and divided it into 4 km × 4 km subfaults. The pressure changes from each sub-fault (Green's function, **G**) are calculated using the same procedure as the forward simulation. In the inversion, considering the filter cutoff (0.033 Hz) is sufficiently low for the *M* ~6 earthquake to neglect the temporal evolution of the rupture propagation across the fault, we assume the ruptures of all sub-faults begin simultaneously (i.e., infinite rupture propagation velocity).

We use the weighting of the smoothing *α* of 0.3, which is determined based on the trade-off between the smoothing weight and the root mean square error (RMSE, Figure S2). The RMSE is defined as:

$$RMSE = \sqrt{\frac{1}{N}\sum_{i=1}^{N}\left(x_i^{\mathrm{obs}} - x_i^{\mathrm{syn}}\right)^2}, \tag{S8}$$

where x_i^{obs} and x_i^{syn} is the *i*-th data of the observed and synthetic waveforms, and *N* is the total number of data samples. We also impose a nonnegativity constraint (Lawson & Hanson, 1974).

Text S3.

This text explains the procedure and results to evaluate the uncertainty of the inversion analysis based on the jackknife, or leave-one-out, approach. Out of the eight APG stations, we exclude one and use the other seven APG stations to estimate the mainshock slip distribution (Figures S4a–S4h). The inversion setting is identical to the original one which used all the APG stations. We then calculate the mean value (μ) and the standard deviation (σ) using these inversion results (Figures S4i-S4j). The possible minimum and maximum slip amounts are evaluated based on the slip distribution with $\mu-1\sigma$ and $\mu+1\sigma$ (Figures S4k–S4l).

As a result of the jackknife test, the constraint of the slip at the northeastern region was not so good, when the B10 station was excluded (Figure S4h), which was located just above the slip area and at the eastern edge of the APG array. This leads to a relatively high standard deviation (Figure S4j). Meanwhile, when the mean slip and standard deviation were calculated based on the inversions using the B10 data (Figures S4a–S4g), the mean slip was very similar to the original inversion result and the deviation was small (Figures S4m–S4p). This means station B10 is important to constrain the slip distribution. Using the mean slip and standard deviation with the jackknife inversions including the B10 data (Figures S4mS4p), the uncertainties of the seismic moment and the area of the slip with large slips ($D > 0.2D_{max}$) were estimated as $8.0–11.6 \times 10^{17}$ Nm and 208–224 km^2.

We further evaluate the uncertainty of the stress drop value, based on the results of the jackknife test (Figure S5). The stress drop distribution calculated by each slip distribution of the jackknife inversions are shown in Figures S5a–S5h. We then calculate the mean stress drop μ and standard deviation σ, using all the jackknife inversion models (Figures S5i–S5l) and using the jackknife inversion models including the B10 data (Figures S5m–S5p). Based on the stress drop distributions with $\mu-1\sigma$ and $\mu+1\sigma$, calculated from the inversions using the B10 data (Figures S5o and S5p), the uncertainty of the stress drop is estimated as 0.44–0.50 MPa.

Text S4.

This text explains the procedure to estimate the radiation energy E_R and radiation efficiency E_R/M_0 (Venkataraman & Kanamori, 2004). The radiation energy E_R is expressed as (Venkataraman & Kanamori, 2004):

$$E_R = \left[\frac{8\pi}{15\rho V_P^5} + \frac{8\pi}{10\rho V_S^5}\right] \int_0^\infty f^2 \left|\hat{\dot{M}}(f)\right|^2 df, \quad \text{(S9)}$$

where ρ is the density, V_P and V_S are the P and S wave velocities, $\hat{\dot{M}}(f)$ is the moment rate spectrum. We here assume the ω^{-2} model (Aki, 1967), for the shape of the moment rate spectrum:

$$\hat{\dot{M}}(f) = \frac{M_0 f_c^2}{f^2 + f_c^2}, \quad \text{(S10)}$$

where f_c is the corner frequency. We set the corner frequency based on the optimum duration estimated from the forward simulation of the ocean-acoustic waves, T_r = 7 s (Figure 4), as f_c = $1/T_r$ = 0.14 Hz. We use the density and P and S wave velocities from the values used for the forward simulation of the dynamic pressure (see Text S1). We used 0.01 to 1 Hz for the integration. As a result, we obtain $E_R = 1.77 \times 10^{12}$ Nm and $E_R/M_0 = 1.87 \times 10^{-6}$.

We also evaluate the uncertainty of the radiated energy and radiation efficiency. Based on the numerical simulation of the ocean-acoustic waves (Figure 4), the simulations with the duration T_r = 6 or 8 s reasonably explained the observed pressure waveforms as well as T_r = 7 s. When assuming T_r = 6 s and 8 s, we obtain $E_R = 2.70 \times 10^{12}$ Nm and 1.23×10^{12} Nm, respectively. Using the smallest value of the possible range of the moment magnitude (M_0 = 8.0×10^{17} Nm, Text S3) and the radiation efficiency with T_r = 6 s, the upper limit of the radiation efficiency was estimated as $E_R/M_0 = 3.33 \times 10^{-6}$. Even if taking account of these uncertainties, these values are consistent with those for tsunami earthquakes estimated from the global M > ~7 event catalog (Ye et al., 2016).

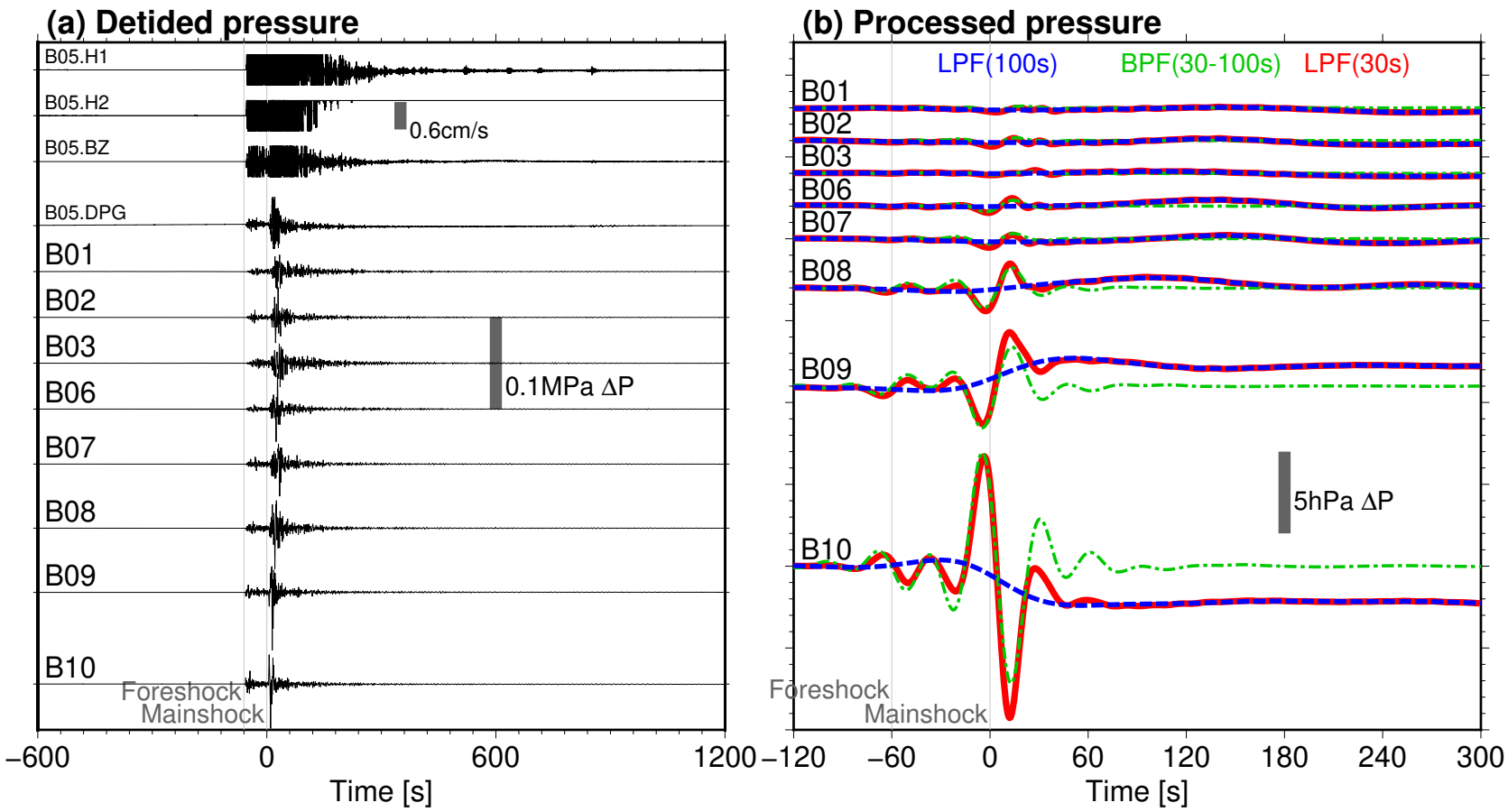

Figure S1. Data processing of the APG records. (a) De-tided waveforms. Seismograms recorded by BBOBS (instrument responses are not corrected) and the pressure recorded by differential pressure gauge (DPG, response-corrected) at station B05 are also shown. (b) Filtered waveforms. Blue dashed, green dashed-and-dotted, and red solid traces denote the lowpass-filtered waveforms (a cutoff of 0.01 Hz), bandpass-filtered waveforms (0.01 to 0.033 Hz), and the lowpass-filtered waveforms (a cutoff of 0.033 Hz), respectively. Note that t = 0 s in the horizontal axis is the origin time. The focal times of the mainshock and foreshocks are also marked. Note that the filters were applied in both the forward and backward directions.

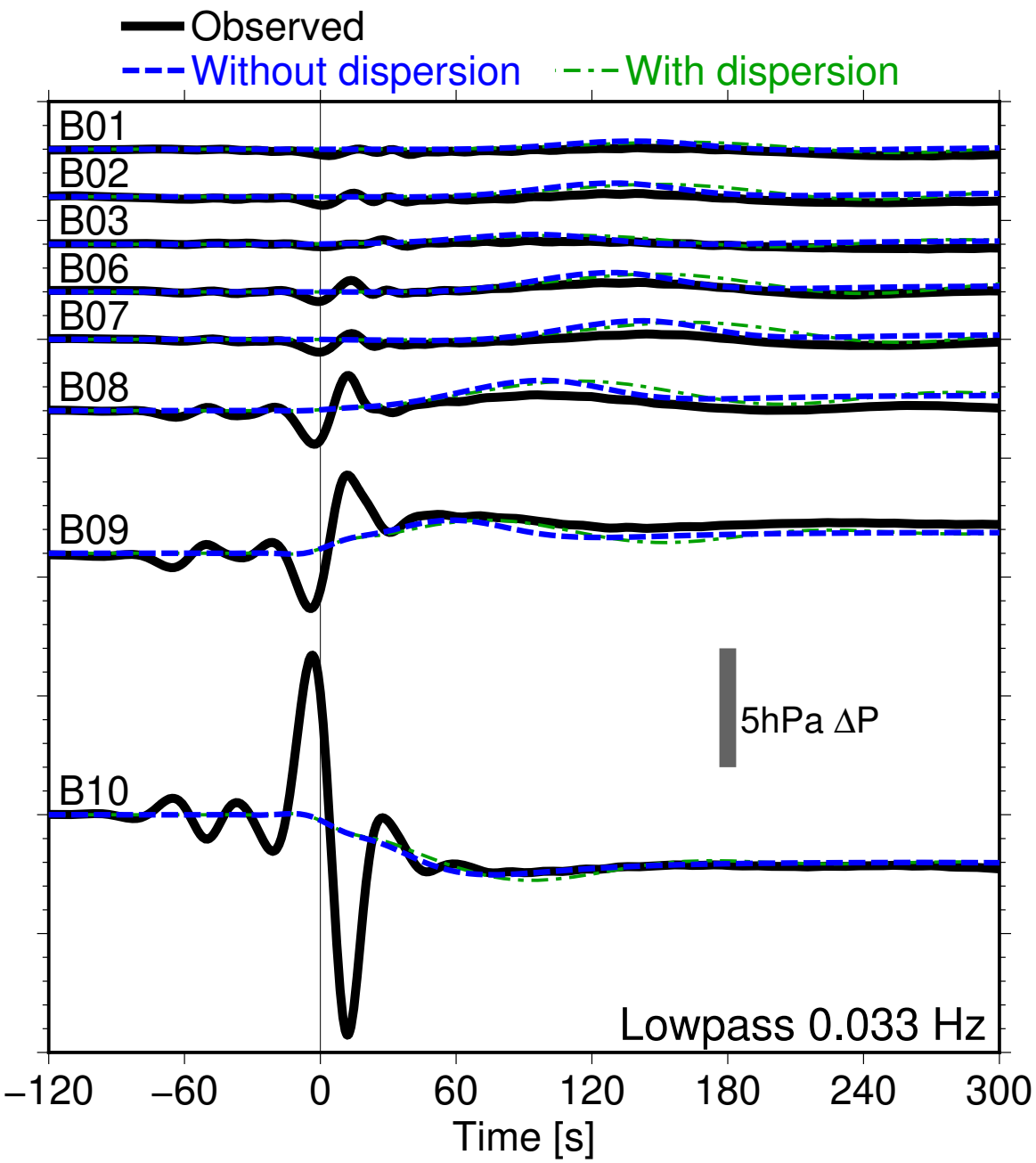

Figure S2. Comparison of the observed (black) and simulated hydrostatic pressure waveforms from the rectangular fault in Figure 1a, considering the dispersion effect or not. Blue traces are the synthetic hydrostatic pressure waveforms without the dispersion effect (identical to those in Figure 1d), and green traces are the waveforms including the dispersion effect. The simulated waveforms are very similar to each other, indicating the effect of the dispersion is very minor.

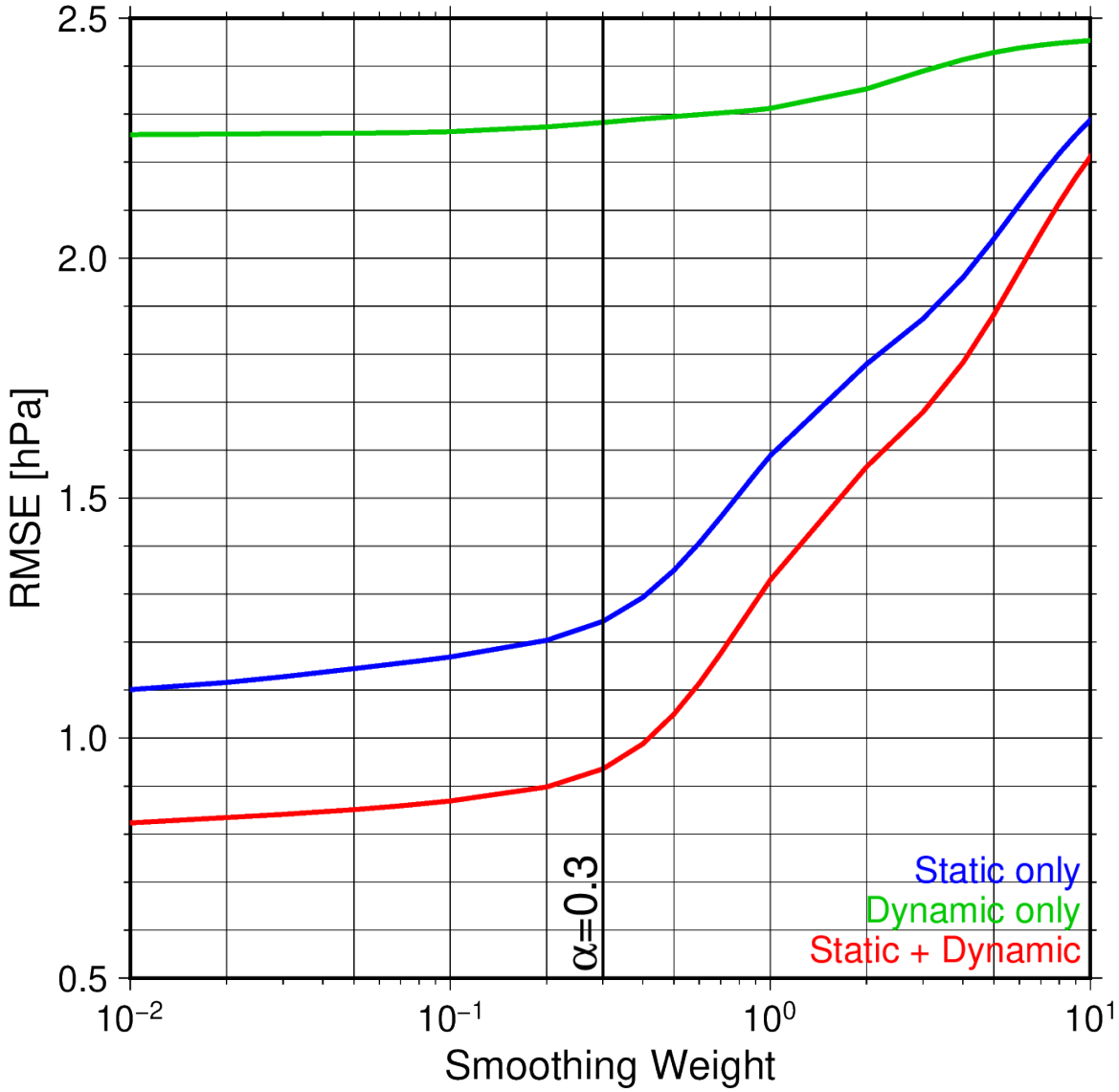

Figure S3. Trade-off curve between the smoothing weight α and the root mean square error (RMSE) for the inversion considering only static (blue), only dynamic (green), and both dynamic and static pressure changes (red). In the inversion, we adopted α = 0.3.

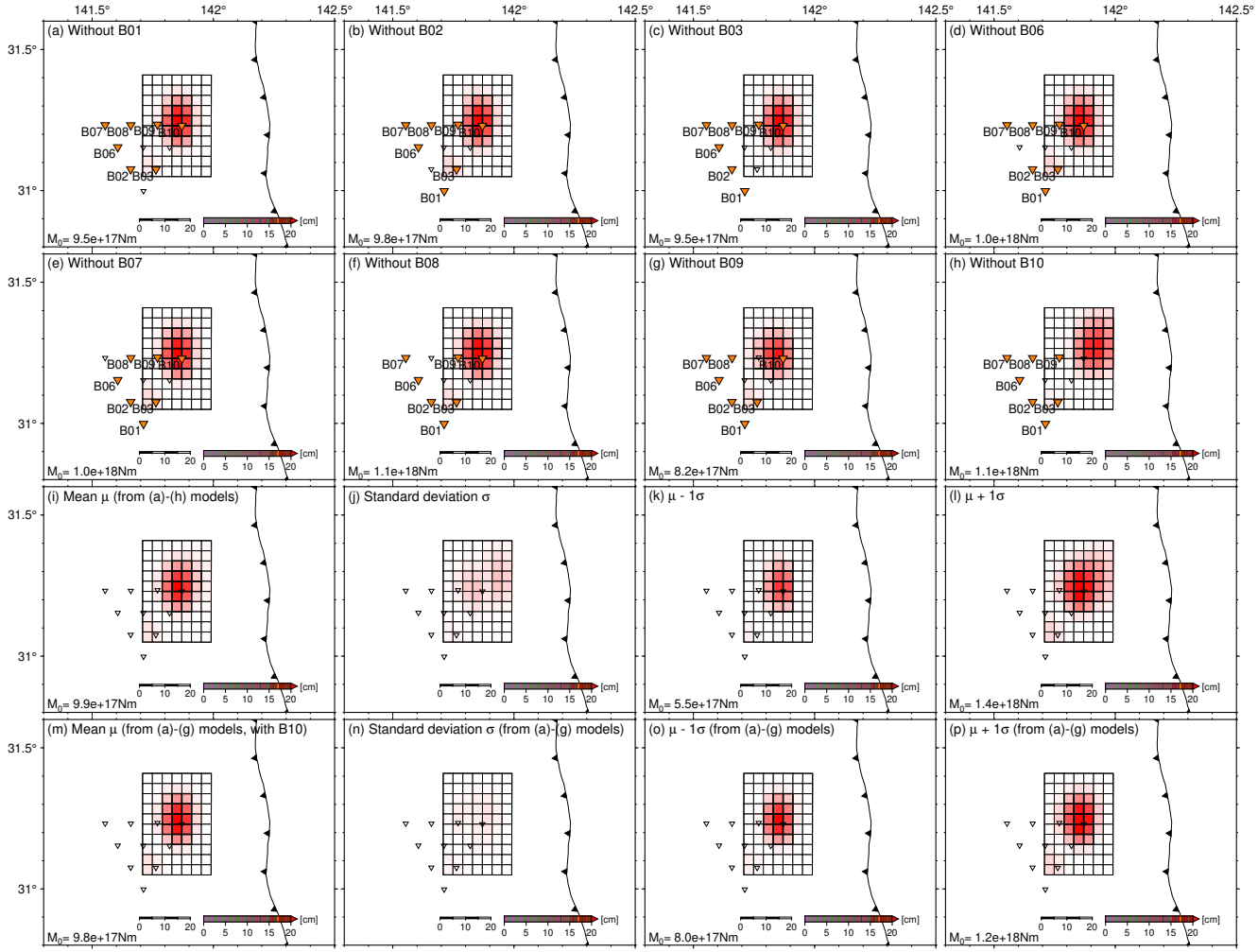

Figure S4. Result of the jackknife inversion test. (a–h) Slip distributions based on the inversions without stations (a) B01, (b) B02, (c) B03, (d) B06, (e) B07, (f) B08, (g) B09, and (h) B10. (i–l) Mean slip μ, standard deviation σ, distribution of $\mu+1\sigma$ and $\mu-1\sigma$, based on all jackknife inversion models ((a)–(h) models), respectively. (m–p) Same as Figure S4i–S4l, but based on the jackknife inversion models using B10 ((a)–(g) models).

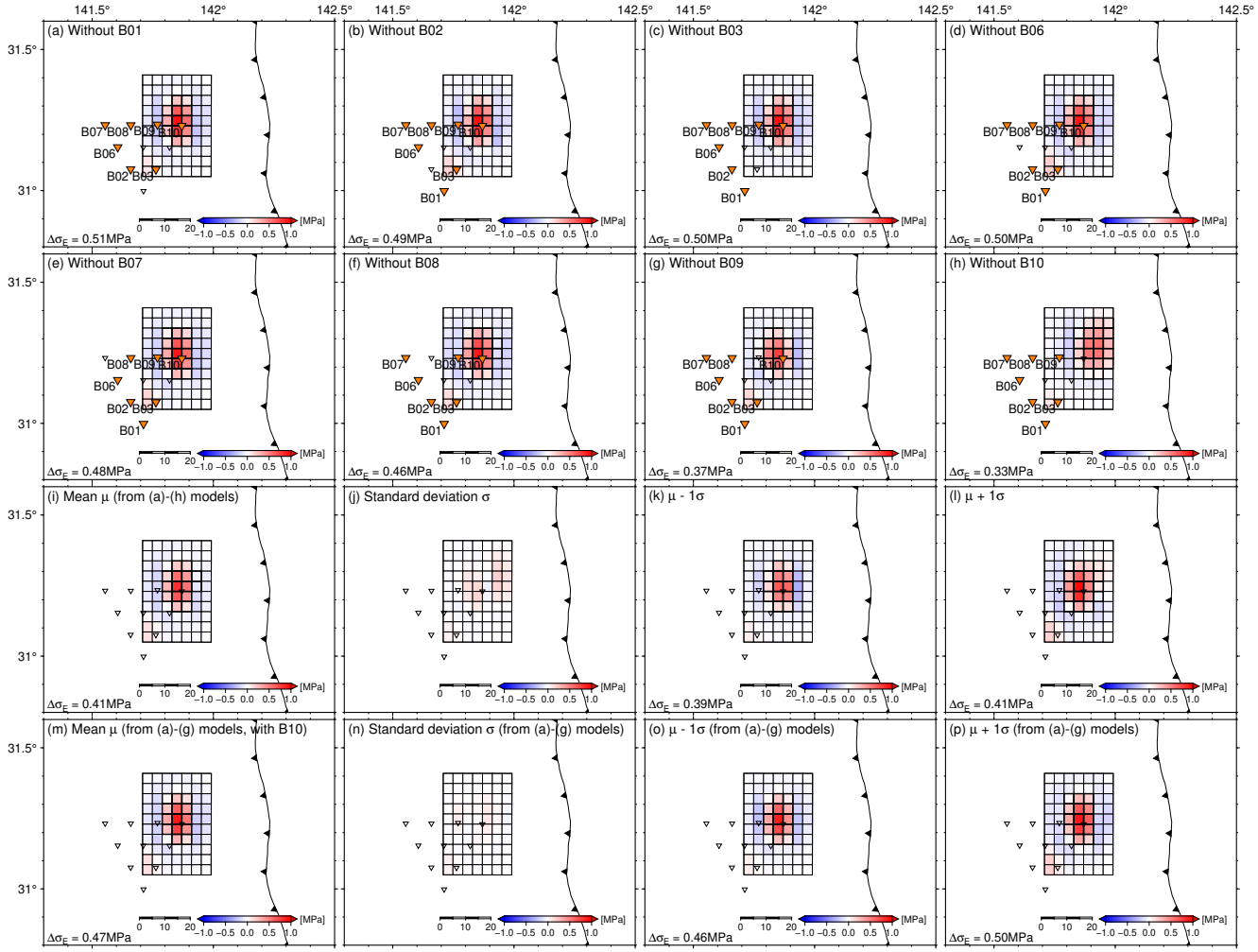

Figure S5. Result of the jackknife inversion test. (a–h) Stress drop distributions based on the inversions without stations (a) B01, (b) B02, (c) B03, (d) B06, (e) B07, (f) B08, (g) B09, and (h) B10. (i–l) Mean stress drop μ, standard deviation σ, distribution of μ+1σ and μ−1σ, based on all jackknife inversion models ((a)–(h) models), respectively. (m–p) Same as Figures S5i–S5l, but based on the jackknife inversion models using B10 ((a)–(g) models)

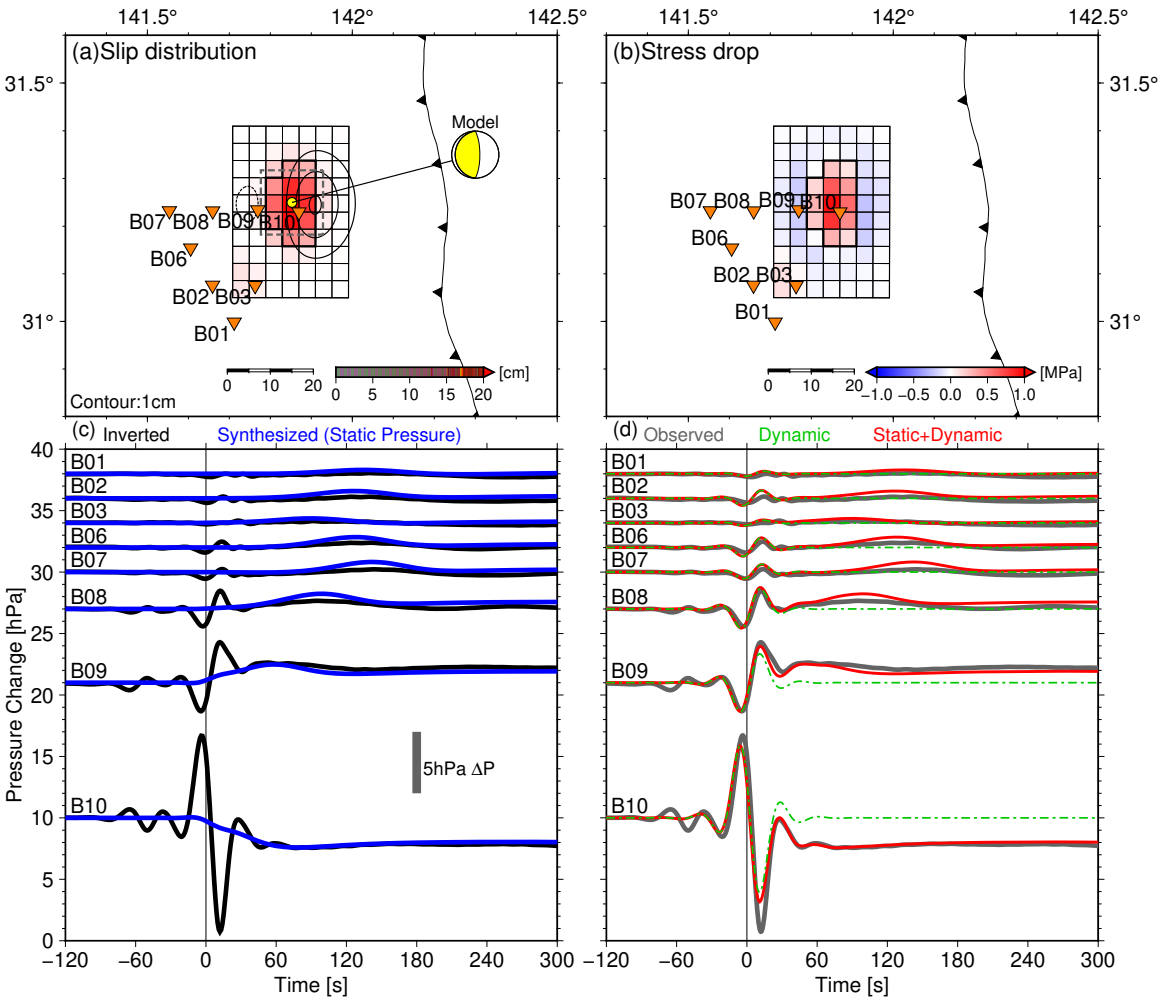

Figure S6. Result of the fault slip inversion using the Green's function incorporating only static pressure change. See Figure 3 for the caption of this figure.

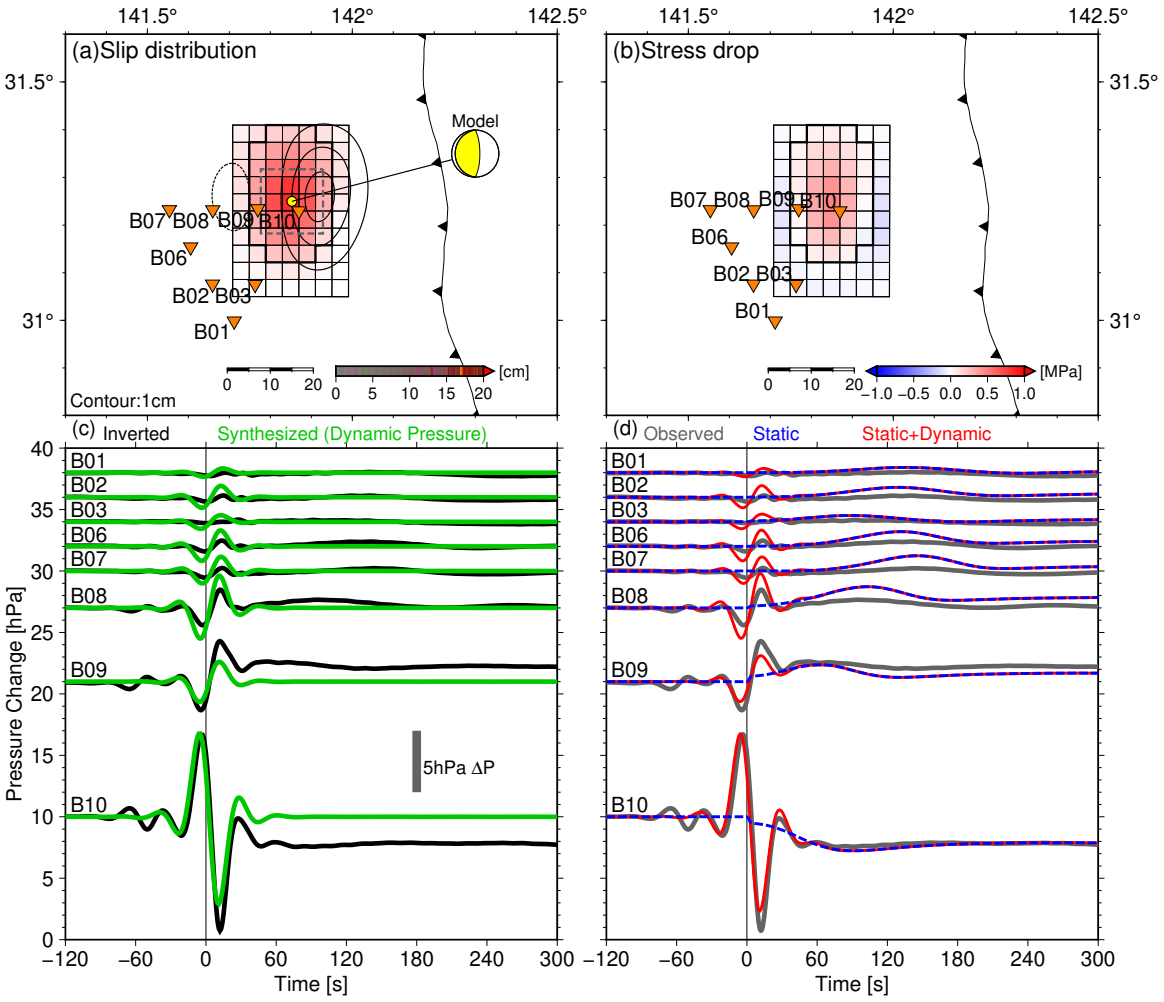

Figure S7. Result of the fault slip inversion using the Green's function incorporating only dynamic pressure changes. See Figure 3 for the caption of this figure.

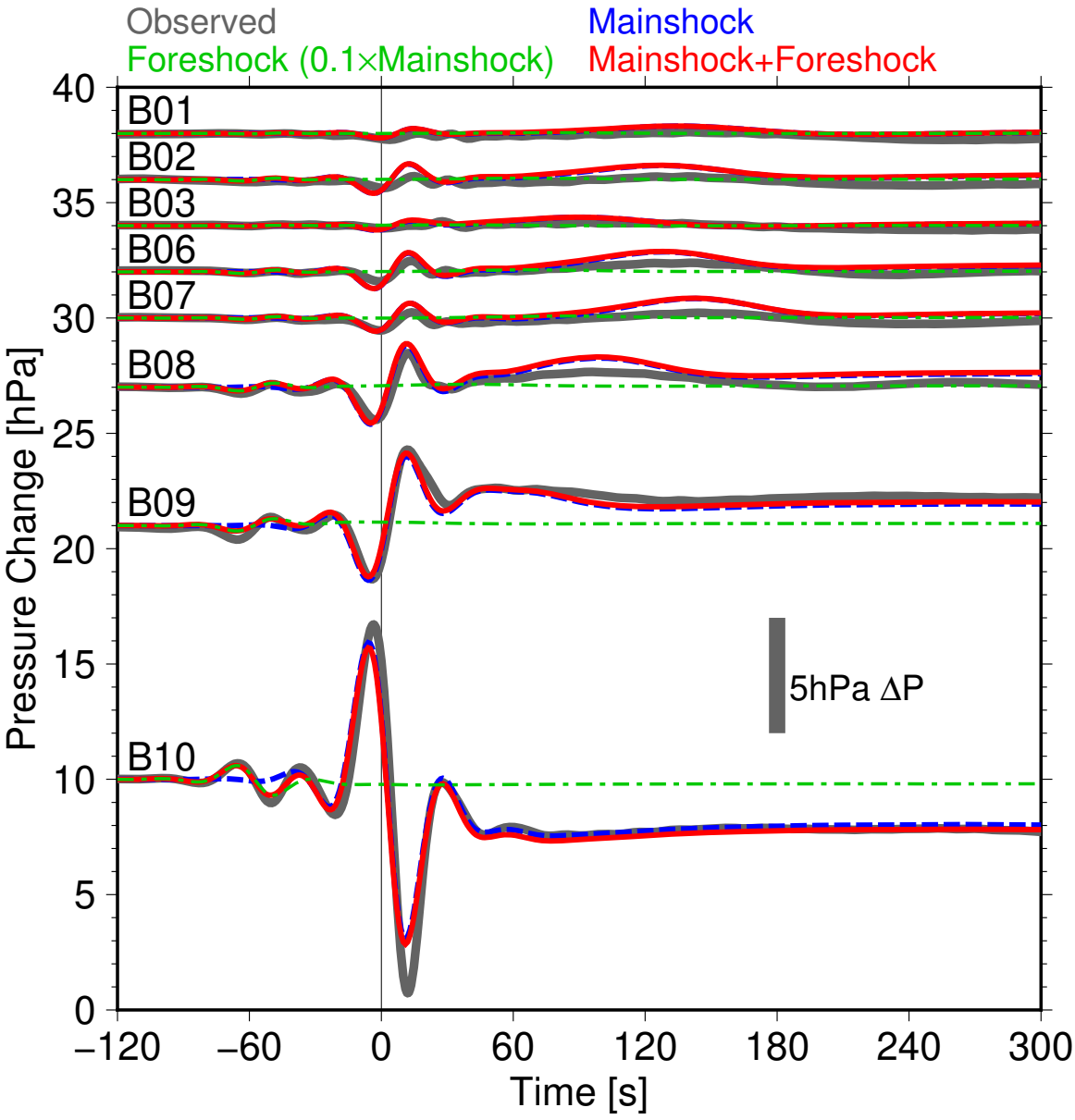

Figure S8. Comparison between the observed waveform (gray) and the forward-calculated waveforms for foreshock (green), mainshock (blue), and both foreshock and mainshock (red), based on the mainshock slip distribution (Figure 3). The red lines in this figure is identical to those in fig. 4 of Fukao et al. (2021).

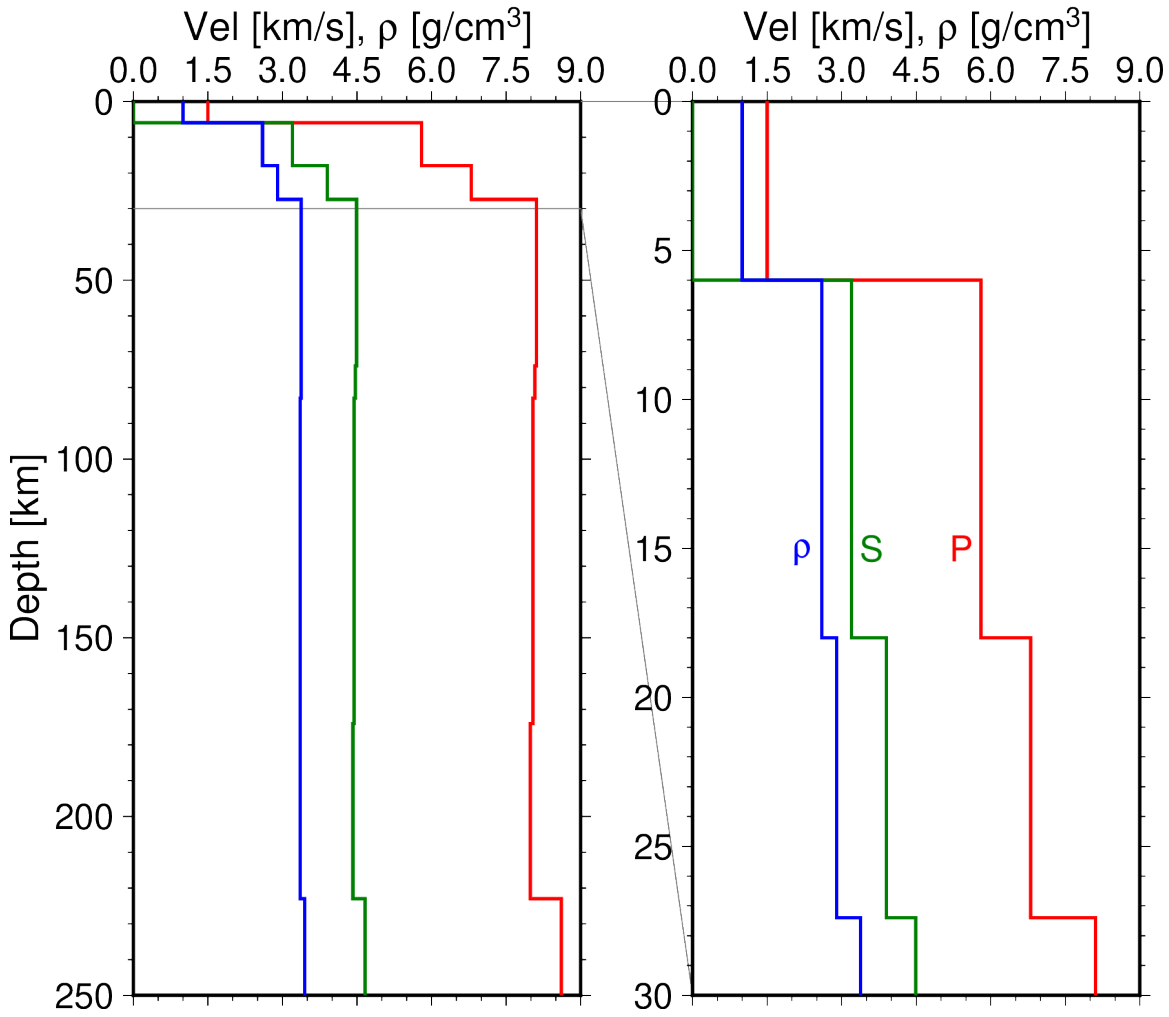

Figure S9. Velocity structure for simulation of the ocean-acoustic wave.

Table S1. Location of the array observation instruments[a]

Station	Instrument[b]	Longitude [°E]	Longitude [°N]	Depth [m]
B01	APG	141.7118	30.9985	5313
B02	APG	141.6590	31.0759	5155
B03	APG	141.7630	31.0754	5601
B04	APG[c]	141.8194	31.1530	4794
B05	BBOBS+DPG	141.7178	31.1536	5427
B06	APG	141.6056	31.1541	4853
B07	APG	141.5536	31.2322	4671
B08	APG	141.6594	31.2319	5089
B09	APG	141.7694	31.2343	5077
B10	APG	141.8699	31.2298	5670

[a]See Fukao et al. (2021) for more details of the observation. Sampling rate of the original APG data is 4 Hz, but the data are sampled to 1 Hz for the present analyses.

[b]APG: Absolute pressure gauges, DPG: Differential pressure gauges, BBOBS: Broadband ocean-bottom seismometer.

[c]No data was obtained due to an error of data logging.